



CHORUS

This is the accepted manuscript made available via CHORUS. The article has been published as:

Measurement of target and double-spin asymmetries for the $e[\overrightarrow{\sigma}]p[\overrightarrow{\sigma}]\rightarrow e\pi^{\{+\}}(n)$ reaction in the nucleon resonance region at low $Q^{\{2\}}$

X. Zheng *et al.* (CLAS Collaboration)

Phys. Rev. C **94**, 045206 — Published 19 October 2016

DOI: [10.1103/PhysRevC.94.045206](https://doi.org/10.1103/PhysRevC.94.045206)

1 Measurement of Target and Double-spin Asymmetries for the $\vec{e}p \rightarrow e\pi^+(n)$ Reaction in the Nucleon 2 Resonance Region at Low Q^2

3 X. Zheng,¹ K.P. Adhikari,^{2,3} P. Bosted,⁴ A. Deur,^{4,1} V. Drozdov,^{5,6} L. El Fassi,^{2,7} Hyekoo Kang,⁸ K. Kovacs,¹ S. Kuhn,³
4 E. Long,⁹ S.K. Phillips,⁹ M. Ripani,⁵ K. Slifer,⁹ L.C. Smith,¹ D. Adikaram,^{3,*} Z. Akbar,¹⁰ M.J. Amarian,³ S.
5 Anefalos Pereira,¹¹ G. Asryan,¹² H. Avakian,⁴ R.A. Badui,¹³ J. Ball,¹⁴ N.A. Baltzell,^{4,15} M. Battaglieri,⁵ V. Batourine,⁴
6 I. Bedlinskiy,¹⁶ A.S. Biselli,^{17,18} W.J. Briscoe,¹⁹ S. Bültmann,³ V.D. Burkert,⁴ D.S. Carman,⁴ A. Celentano,⁵ S. Chandavar,²⁰
7 G. Charles,²¹ J.-P. Chen,⁴ T. Chetry,²⁰ Seonho Choi,⁸ G. Ciullo,²² L. Clark,²³ L. Colaneri,^{24,25} P.L. Cole,²⁶ N. Compton,²⁰
8 M. Contalbrigo,²² V. Crede,¹⁰ A. D'Angelo,^{24,25} N. Dashyan,¹² R. De Vita,⁵ E. De Sanctis,¹¹ C. Djalali,¹⁵ G.E. Dodge,³
9 R. Dupre,²¹ H. Egiyan,^{4,9} A. El Alaoui,²⁷ L. Elouadrhiri,⁴ P. Eugenio,¹⁰ E. Fanchini,⁵ G. Fedotov,^{15,6} R. Fersch,²⁸ A. Filippi,²⁹
10 J.A. Fleming,³⁰ N. Gevorgyan,¹² Y. Ghandilyan,¹² G.P. Gilfoyle,³¹ K.L. Giovanetti,³² F.X. Girod,^{4,14} C. Gleason,¹⁵
11 E. Golovach,⁶ R.W. Gothe,¹⁵ K.A. Griffioen,³³ M. Guidal,²¹ N. Guler,^{3,†} L. Guo,^{13,4} C. Hanretty,^{1,*} N. Harrison,⁴
12 M. Hattawy,⁷ K. Hicks,²⁰ M. Holtrop,⁹ S.M. Hughes,³⁰ Y. Ilieva,^{15,19} D.G. Ireland,²³ B.S. Ishkhanov,⁶ E.L. Isupov,⁶
13 D. Jenkins,³⁴ H. Jiang,¹⁵ H.S. Jo,²¹ S. Joosten,³⁵ D. Keller,¹ G. Khachatryan,¹² M. Khandaker,^{26,36} A. Kim,³⁷
14 W. Kim,³⁸ F.J. Klein,³⁹ V. Kubarovsky,^{4,40} L. Lanza,^{24,25} P. Lenisa,²² K. Livingston,²³ I. J. D. MacGregor,²³
15 N. Markov,³⁷ B. McKinnon,²³ M. Mirazita,¹¹ V. Mokeev,^{4,6} A. Movsisyan,²² E. Munevar,^{4,19} C. Munoz Camacho,²¹ G.
16 Murdoch,²³ P. Nadel-Turonski,^{4,39} L.A. Net,¹⁵ A. Ni,³⁸ S. Niccolai,²¹ G. Niculescu,³² I. Niculescu,³² M. Osipenko,⁵
17 A.I. Ostrovidov,¹⁰ M. Paolone,³⁵ R. Paremuzyan,⁹ K. Park,^{4,38} E. Pasyuk,⁴ P. Peng,¹ S. Pisano,¹¹ O. Pogorelko,¹⁶
18 J.W. Price,⁴¹ A.J.R. Puckett,³⁷ B.A. Raue,^{13,4} A. Rizzo,^{24,25} G. Rosner,²³ P. Rossi,^{4,11} P. Roy,¹⁰ F. Sabatié,¹⁴
19 C. Salgado,³⁶ R.A. Schumacher,¹⁸ Y.G. Sharabian,⁴ Iu. Skorodumina,^{15,6} G.D. Smith,³⁰ D. Sokhan,²³ N. Sparveris,³⁵
20 I. Stankovic,³⁰ I.I. Strakovsky,¹⁹ S. Strauch,^{15,19} M. Taiuti,^{5,42} Ye Tian,¹⁵ M. Ungaro,^{4,37} H. Voskanyan,¹² E. Voutier,²¹
21 N.K. Walford,³⁹ D.P. Watts,³⁰ X. Wei,⁴ L.B. Weinstein,³ M.H. Wood,^{43,15} N. Zachariou,³⁰ J. Zhang,⁴ and I. Zonta^{24,25}

22 (The CLAS Collaboration)

23 ¹University of Virginia, Charlottesville, Virginia 22901, USA

24 ²Mississippi State University, Mississippi State, Mississippi 39762, USA

25 ³Old Dominion University, Norfolk, Virginia 23529, USA

26 ⁴Thomas Jefferson National Accelerator Facility, Newport News, Virginia 23606, USA

27 ⁵INFN, Sezione di Genova, 16146 Genova, Italy

28 ⁶Skobeltsyn Institute of Nuclear Physics, Lomonosov Moscow State University, 119234 Moscow, Russia

29 ⁷Argonne National Laboratory, Argonne, Illinois 60439, USA

30 ⁸Seoul National University, Seoul, Korea

31 ⁹University of New Hampshire, Durham, New Hampshire 03824, USA

32 ¹⁰Florida State University, Tallahassee, Florida 32306, USA

33 ¹¹INFN, Laboratori Nazionali di Frascati, 00044 Frascati, Italy

34 ¹²Yerevan Physics Institute, 375036 Yerevan, Armenia

35 ¹³Florida International University, Miami, Florida 33199, USA

36 ¹⁴CEA, Centre de Saclay, Irfu/Service de Physique Nucléaire, 91191 Gif-sur-Yvette, France

37 ¹⁵University of South Carolina, Columbia, South Carolina 29208, USA

38 ¹⁶Institute of Theoretical and Experimental Physics, Moscow, 117259, Russia

39 ¹⁷Fairfield University, Fairfield, Connecticut 06824, USA

40 ¹⁸Carnegie Mellon University, Pittsburgh, Pennsylvania 15213, USA

41 ¹⁹The George Washington University, Washington, DC 20052, USA

42 ²⁰Ohio University, Athens, Ohio 5701, USA

43 ²¹Institut de Physique Nucléaire, CNRS/IN2P3 and Université Paris Sud, Orsay, France

44 ²²INFN, Sezione di Ferrara, 44100 Ferrara, Italy, USA

45 ²³University of Glasgow, Glasgow G12 8QQ, United Kingdom

46 ²⁴INFN, Sezione di Roma Tor Vergata, 00133 Rome, Italy

47 ²⁵Universita' di Roma Tor Vergata, 00133 Rome Italy

48 ²⁶Idaho State University, Pocatello, Idaho 83209, USA

49 ²⁷Universidad Técnica Federico Santa María, Casilla 110-V Valparaíso, Chile

50 ²⁸Christopher Newport University, Newport News, Virginia 23606, USA

51 ²⁹INFN, Sezione di Torino, 10125 Torino, Italy

52 ³⁰Edinburgh University, Edinburgh EH9 3JZ, United Kingdom

53 ³¹University of Richmond, Richmond, Virginia 23173, USA

54 ³²James Madison University, Harrisonburg, Virginia 22807, USA

55 ³³College of William and Mary, Williamsburg, Virginia 23187, USA

56 ³⁴Virginia Tech, Blacksburg, Virginia 24061, USA

57 ³⁵Temple University, Philadelphia, Pennsylvania 19122, USA

58 ³⁶Norfolk State University, Norfolk, Virginia 23504, USA

³⁷University of Connecticut, Storrs, Connecticut 06269, USA

³⁸Kyungpook National University, Daegu 702-701, Republic of Korea

³⁹Catholic University of America, Washington, D.C. 20064, USA

⁴⁰Rensselaer Polytechnic Institute, Troy, New York 12180, USA

⁴¹California State University, Dominguez Hills, Carson, California 90747, USA

⁴²Università di Genova, Dipartimento di Fisica, 16146 Genova, Italy

⁴³Canisius College, Buffalo, New York 14208, USA

(Dated: September 22, 2016)

We report measurements of target- and double-spin asymmetries for the exclusive channel $\vec{e}\vec{p} \rightarrow e\pi^+(n)$ in the nucleon resonance region at Jefferson Lab using the CEBAF Large Acceptance Spectrometer (CLAS). These asymmetries were extracted from data obtained using a longitudinally polarized NH_3 target and a longitudinally polarized electron beam with energies 1.1, 1.3, 2.0, 2.3 and 3.0 GeV. The new results are consistent with previous CLAS publications but are extended to a low Q^2 range from 0.0065 to 0.35 $(\text{GeV}/c)^2$. The Q^2 access was made possible by a custom-built Cherenkov detector that allowed the detection of electrons for scattering angles as low as 6° . These results are compared with the unitary isobar models JANR and MAID, the partial-wave analysis prediction from SAID and the dynamic model DMT. In many kinematic regions our results, in particular results on the target asymmetry, help to constrain the polarization-dependent components of these models.

PACS numbers: 13.60.Le, 13.88.+e, 14.20.Gk

I. PHYSICS MOTIVATION

The perturbative nature of the strong interaction at small distances – often referred to as “asymptotic freedom” – was established more than 30 years ago and provided strong support for Quantum Chromodynamics (QCD) to be accepted as the correct theory for strong interactions [1, 2]. On the other hand, calculations at long-distances are still beyond reach because of the non-perturbative nature at this scale. As a result, we are still far away from being able to describe the strong force as it manifests itself in the structure of baryons and mesons [3][4].

A fundamental approach to resolve this difficulty is to develop accurate numerical simulations of QCD on the Lattice, for recent reviews see [5, 6]. However Lattice QCD methods are difficult to apply to light-quark systems such as the nucleon. Alternatively, hadron models with effective degrees of freedom have been constructed to interpret data. One example is the chiral perturbation theory [7, 8], which is constrained only by the symmetry properties of QCD. The constituent quark model, though not fully understood, is one successful example that works almost everywhere from hadron spectroscopy to deep inelastic scattering [9, 10]. Predictions for the scattering amplitudes and polarization-dependent asymmetries exist for many resonances within the framework of the relativistic constituent quark model (RCQM) [11] and the single quark transition model (SQTm) [12].

The comparison between these predictions and experimental results, on the other hand, is not straightforward. This is because the experimentally measured cross sections and asymmetries are usually complicated combinations of resonant and non-resonant amplitudes and couplings, and their

interference terms. To compare with theories, partial wave analyses are often used to extract these amplitudes and resonance couplings from data. Once comparisons can be made, data are used to provide inputs for constructing or adjusting meson production mechanisms in theories and models, such as proper treatment of the hadronic final state and implementation of the non-resonant part of the meson production amplitude. These mechanisms are usually not included in quark models. Examples of phenomenological partial wave analyses that can benefit from more data are MAID [13], JANR [14], SAID [15], and the DMT [16] models. Electron-scattering data used to test these calculations include primarily $N - N^*$ transition form factors and response functions for meson production reactions obtained from Jefferson Lab (JLab), MAMI and MIT-Bates. Recently, polarization observables such as double spin asymmetries and target spin asymmetries for pion electro-production from the proton have made the beam- and target-helicity response functions accessible [17–20], providing a new approach to testing models and to a greater understanding of the baryon resonance structure. As an example, the MAID model was based mostly on unpolarized data and is only recently being tested extensively against double polarization asymmetries. In general, polarization observables provide an important constraint on the understanding of the underlying helicity response functions or interference terms in $N \rightarrow \Delta$ and $N \rightarrow N^*$ resonances.

Compared to the proton, existing data on neutron excitation were particularly sparse. Neutron data have recently become available from JLab [21, 22], which make it possible to test the isospin structure of models such as RCQM and SQTm. The neutron data will be valuable to the development of many phenomenological analyses as well because they need to incorporate double polarization asymmetry data for all pion production channels from both the proton and the neutron in order to perform the full isospin decomposition.

In addition, data at very low Q^2 values are often desired for testing the chiral perturbation theory and to study the transition from virtual photons to the real photon point ($Q^2 = 0$). Here, Q^2 is defined as $Q^2 \equiv -q^2$, where $q \equiv (\nu, \vec{q})$ is the

* Current address: Thomas Jefferson National Accelerator Facility, Newport News, Virginia 23606, USA

† Current address: Los Alamos National Laboratory, Los Alamos, New Mexico 87544, USA

four-momentum transferred from the incident electron to the target and

$$\nu \equiv E - E' \quad (1)$$

with E and E' the incident and the scattered electron's energies, respectively. At low energy transfers $\nu < 2$ GeV the most prominent resonances are the $\Delta(1232)3/2^+$, $N(1520)3/2^-$ and $N(1680)5/2^+$ [11]. For the $N(1520)3/2^-$ and $N(1680)5/2^+$, their amplitudes at large Q^2 are determined by perturbative QCD and hadron helicity conservation. It is expected in this region that $A^N \rightarrow 1$, where A^N is the virtual photon helicity asymmetry defined as:

$$A^N = \frac{|A_{1/2}|^2 - |A_{3/2}|^2}{|A_{1/2}|^2 + |A_{3/2}|^2}, \quad (2)$$

with $A_{1/2,3/2}$ the scattering amplitudes and the subscripts indicate the total spin projection of the virtual photon and the nucleon target along the virtual photon's momentum. However, data using real photons show a strong helicity-3/2 dominance and $A^N \rightarrow -1$ [23]. This indicates that A^N for these two resonances must cross zero at some intermediate Q^2 and there have been calculations for the Q^2 -dependence of A^N from various models [11, 12, 24]. For pion electroproduction, the double spin asymmetry is dominated by A^N [17] and thus data on this observable will allow us to test a possible sign flip for the $N(1520)3/2^-$ and $N(1680)5/2^+$ resonances. Data on the double spin asymmetry of pion photoproduction have recently become available from the CBELSA/TAPS Collaboration [25] and are also expected from JLab experiments [26][27][28], all used the frozen spin target with a longitudinal polarization and a circularly polarized photon beam. These photoproduction data will further test the transition to the real photon point.

A. Formalism for Pion Electroproduction

Figure 1 shows the kinematics of single pion production in the Born approximation: the electron transfers a virtual photon γ^* of four-momentum $q \equiv (\nu, \vec{q})$ to the target nucleon N which forms a nucleon resonance. The resonance then decays into a pion and another particle X . Two planes are used to describe this process: the scattering (leptonic) plane defined by the incoming and outgoing electrons' momenta \vec{k} and \vec{k}' , and the reaction (hadronic) plane defined by the momentum of the virtual photon \vec{q} and the momentum of the outgoing pion \vec{p}_π .

The reaction is usually described in terms of Q^2 , the invariant mass W of the γ^*N system (which is also the πX system), and two angles θ^* and ϕ^* . Here, θ^* is the angle formed by \vec{q} and \vec{p}_π , and ϕ^* is the angle formed by rotating the leptonic plane to the hadronic plane. If one defines the γ^*N center of mass (CM) frame with \hat{z} pointing along \vec{q} , \hat{y} along $\vec{q} \times \vec{k}$, then θ^* and ϕ^* are the polar and the azimuthal angles of the emitted pion. The energy transfer is related to Q^2 and W via

$$\nu = \frac{W^2 + Q^2 - M^2}{2M}, \quad (3)$$

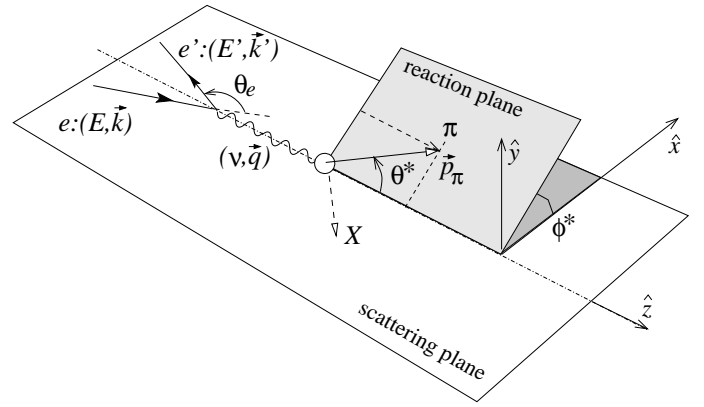


FIG. 1. Kinematics of single pion electro-production. The Lorentz boost associated with the transformation from the laboratory to the CM frame of the γ^*N system is along the momentum transfer \vec{q} , where the coordinates \hat{x} , \hat{y} , \hat{z} of the CM frame are defined in this picture.

with M the nucleon mass. The differential cross section for the reaction $e\bar{N} \rightarrow e\pi(X)$ with longitudinally polarized beam and target can be written in the following form

$$\frac{d^5\sigma_h}{dE_{e'}d\Omega_{e'}d\Omega_\pi^*} = \Gamma \frac{d\sigma_h}{d\Omega_\pi^*}, \quad (4)$$

with

$$\frac{d\sigma_h}{d\Omega_\pi^*} = \frac{d\sigma_0}{d\Omega_\pi^*} + P_b \frac{d\sigma_e}{d\Omega_\pi^*} + P_t \frac{d\sigma_t}{d\Omega_\pi^*} + P_b P_t \frac{d\sigma_{et}}{d\Omega_\pi^*} \quad (5)$$

where P_b and P_t are respectively the polarizations of the electron beam and the target along the beam direction, σ_0 is the unpolarized cross section, and σ_e , σ_t and σ_{et} are the polarized cross section terms when beam, target, and both beam and target are polarized. Note that the differential cross sections on the right-hand side of Eq. (5) are defined in the CM frame of the γ^*N system, as indicated by the asterisk in the pion's solid angle. The virtual photon flux is

$$\Gamma = \frac{\alpha k_\gamma^{\text{lab}}}{2\pi^2 Q^2} \frac{E'}{E} \frac{1}{1 - \epsilon}, \quad (6)$$

where α is the electromagnetic coupling constant, $k_\gamma^{\text{lab}} = (W^2 - M^2)/2M$ is the photon equivalent energy in the laboratory frame, i.e. the energy needed by a real photon to excite the nucleon to an invariant mass W . The virtual photon polarization is given by

$$\epsilon = \left[1 + \frac{2|\vec{q}|^2}{Q^2} \tan^2 \frac{\theta_e}{2} \right]^{-1}, \quad (7)$$

where θ_e is the angle between the incident and outgoing electrons in the laboratory frame. The Q^2 can be calculated as

$$Q^2 = 4EE' \sin^2 \frac{\theta_e}{2}. \quad (8)$$

211 To evaluate the pion's kinematics in the CM frame of the
 212 γ^*N system, we relate a laboratory-frame 4-momentum vec-
 213 tor p^μ to the CM-frame p_{cm}^μ via a Lorentz boost with $\vec{\beta} =$
 214 $\hat{z}|\vec{q}|/(\nu + M)$ and $\gamma = (\nu + M)/W$:

$$215 \quad p_{\text{cm}}^0 = \gamma p^0 - \gamma\beta p^z, \quad (9)$$

$$216 \quad p_{\text{cm}}^x = p^x, \quad (10)$$

$$217 \quad p_{\text{cm}}^y = p^y, \quad (11)$$

$$218 \quad p_{\text{cm}}^z = -\gamma\beta p^0 + \gamma p^z. \quad (12)$$

219 Specifically, we have for the virtual photon:

$$220 \quad |\vec{q}_{\text{cm}}| = \frac{M}{W}|\vec{q}|, \quad (13)$$

$$221 \quad \nu_{\text{cm}} = \frac{\nu M - Q^2}{W}. \quad (14)$$

222 For the pion

$$223 \quad E_{\text{cm},\pi} = \gamma(E_\pi - \beta|\vec{p}_\pi| \cos\theta_\pi), \quad (15)$$

$$224 \quad p_{z,\text{cm},\pi} = \gamma(|\vec{p}_\pi| \cos\theta_\pi - \beta E_\pi), \quad (16)$$

225 where $\theta_\pi = \arccos[(\vec{q} \cdot \vec{p}_\pi)/(|\vec{q}||\vec{p}_\pi|)]$ is the angle between the
 226 pion momentum and \vec{q} in the laboratory frame, and E_π is the
 227 pion energy again in the laboratory frame. The polar angle of
 228 the pion in the CM frame is given by

$$229 \quad \theta^* = \arccos\left[\frac{p_{z,\text{cm},\pi}}{\sqrt{E_{\text{cm},\pi}^2 - m_\pi^2}}\right] \quad (17)$$

230 where m_π is the pion mass. The azimuthal angle of the pion
 231 is the same in the laboratory and the CM frame, given by

$$232 \quad \phi^* = \arccos\left[\frac{\vec{a} \cdot \vec{b}}{|\vec{a}||\vec{b}|}\right] \quad (18)$$

233 with $\vec{a} \equiv \vec{q} \times \vec{k}$ and $\vec{b} \equiv \vec{q} \times \vec{p}_\pi$. In this paper, the range of ϕ^*
 234 is defined from 0 to 2π , i.e. a shift of 2π is added to ϕ^* if the
 235 result from Eq. (18) is negative.

236 The beam, target and double beam-target asymmetries are

$$237 \quad A_{LU} = \frac{\sigma_e}{\sigma_0}, \quad (19)$$

$$238 \quad A_{UL} = \frac{\sigma_t}{\sigma_0}, \quad (20)$$

$$239 \quad A_{LL} = -\frac{\sigma_{et}}{\sigma_0}, \quad (21)$$

240 where each cross section σ stands for the $d\sigma/d\Omega_\pi^*$ of Eq. (5).
 241 Note that we have adopted an extra minus sign in the defini-
 242 tion of A_{LL} to be consistent with Eq. (2) and previous CLAS
 243 publications [17–19].

244 In this paper, we report on results of both A_{UL} and A_{LL}
 245 extracted from the JLab CLAS EG4 [29, 30] data. The beam
 246 asymmetry A_{LU} was also extracted from the data, but was
 247 used only as a cross-check of the beam helicity and is not
 248 presented here. These results are available for download from
 249 the CLAS database.

250 B. Previous Data

251 The first double-spin asymmetry for the π^+n channel was
 252 published based on the CLAS EG1a data with a 2.6 GeV
 253 beam, for a Q^2 range from 0.35 to 1.5 (GeV/c)² [17, 18]. The
 254 $\vec{e}\vec{p} \rightarrow e'p(\pi^0)$ channel was analyzed for the $\Delta(1232)3/2^+$
 255 region using the same dataset [19]. Similar analysis using the
 256 CLAS EG1b data has been completed [20, 22], in which the
 257 target and the double spin asymmetries were extracted from
 258 both the $\vec{e}\vec{p} \rightarrow e'\pi^+(n)$ and $\vec{e}\vec{n} \rightarrow e'\pi^-p$ channels using 1.6
 259 to 5.7 GeV beams with Q^2 as low as 0.1 (GeV/c)².

260 II. THE JLAB CLAS EG4 EXPERIMENT

261 The main physics goal of the CLAS EG4 experiment [29,
 262 30] was to measure the inclusive spin structure functions on
 263 the proton and the deuteron, and to extract the generalized
 264 Gerasimov-Drell-Hearn (GDH) sum near the photon point.
 265 The original GDH sum rule [31, 32], defined for real photons,
 266 is a fundamental prediction on the nucleon's spin structure
 267 that relates the helicity-dependent total photo-absorption cross
 268 section to the nucleon anomalous magnetic moment. The defini-
 269 tion of the GDH sum has been generalized to virtual pho-
 270 tons [33, 34], and the value of the generalized GDH sum at
 271 low Q^2 has been predicted in the chiral perturbation theory.
 272 Similar to the pion production results presented here, the goal
 273 of the EG4's inclusive analysis is to test the chiral perturba-
 274 tion theory prediction and to compare the extrapolation to the
 275 $Q^2 = 0$ point with the GDH sum rule of the real photon.

276 The experiment was carried out in 2006 in experimental
 277 Hall B of JLab. Inclusive data were collected in the range
 278 $1 < W < 2$ GeV/c² and Q^2 down to 0.015 (GeV/c)² [35],
 279 using six beam energies (1.1, 1.3, 1.5, 2.0, 2.3, 3.0 GeV) on
 280 a polarized NH₃ target and two energies (1.3, 2.0 GeV) on a
 281 polarized ND₃ target. The average polarizations of NH₃ and
 282 ND₃ typically ranged within (75 – 90)% and (30 – 45)%,
 283 respectively. For the exclusive channel, only NH₃ data with
 284 beam energies of 1.1, 1.3, 2.0, 2.3, and 3.0 GeV were analyzed
 285 with the lowest Q^2 being 0.0065 (GeV/c)². The 1.5 GeV en-
 286 ergy data were excluded because they were taken for run com-
 287 missioning purpose and had limited statistics. For ND₃ data,
 288 the target spin direction was not flipped during the run, which
 289 makes it impossible to extract A_{UL} nor the complete informa-
 290 tion on A_{LL} from the exclusive channel.

291 A. The CLAS Detector

292 The CEBAF Large Acceptance Spectrometer (CLAS) was
 293 used to detect scattered particles [36]. Figure 2 shows the ba-
 294 sic structure of CLAS during EG4 with the polarized target
 295 installed. CLAS is an almost hermetic detector, optimized for
 296 the measurement of multi-particle final states in a large mo-
 297 mentum region. The detector design is based on a toroidal
 298 magnet made by six superconducting coils arranged around
 299 the beam line to produce a field pointing primarily in the az-
 300 imuthal direction. The field direction can be set such that

301 the scattered negatively-charged particles can be either bent
 302 away from the beamline (“electron outbending”) or towards it
 303 (“electron inbending”). The detector itself is composed of six
 304 independent magnetic spectrometers, referred to as six “sec-
 305 tors”, with a common target, trigger, and data acquisition sys-
 306 tem. Each sector is equipped with a three-layer drift cham-
 307 ber system (DC) for momentum and tracking determination, a
 308 time-of-flight (TOF) counter, a Cherenkov Counter (CC) and
 309 a double-layer Electromagnetic Calorimeter (EC). The TOF,
 310 CC and the EC systems are primarily used for determining
 311 the particle type.

312 In order to reach very low Q^2 while retaining the high beam
 313 energy needed to measure the GDH sum, a small scattering
 314 angle was necessary. This was achieved by running the CLAS
 315 torus magnet in the electron-outbending configuration. Al-
 316 though the standard CLAS Cherenkov detector geometrically
 317 reaches an 8° scattering angle [37], its structure is not ideal
 318 for collecting the Cherenkov light for outbending electrons.
 319 Therefore, for the EG4 experiment, a new Cherenkov detector
 320 was built by the INFN-Genova group and installed in sector 6,
 321 as shown in Fig. 2. It was designed to reach 6° scattering
 322 angle by optimizing the light collection for the electron-out-
 323 bending configuration. Due to the very high counting rates at such
 324 low scattering angles, instrumenting only one CLAS sector was
 325 sufficient for the experiment. The new Cherenkov detector
 326 used the same radiator gas (C_4F_{10}) and the gas flow control
 327 system used in the standard CLAS Cherenkov. It consisted
 328 of 11 segments, each equipped with a pair of light-weight
 329 spherical mirrors, see Fig. 3. The mirrors were constructed
 330 following [38], by shaping a plexiglass layer onto a spheri-
 331 cal mould, then gluing onto it a sandwich of carbon fiber and
 332 honeycomb, and finally evaporating a thin layer of aluminum
 333 onto the plexiglass. Each mirror reflected the light towards a
 334 light collector made of two pieces, an entrance section with
 335 the approximate shape of a truncated pyramid and a guiding
 336 section cylindrical in shape such as to match the circular pho-
 337 to-cathode. Each light collector was made of plexiglass with
 338 aluminum evaporated on the internal surface. The entrance
 339 section was built by a no-contact technique, where the plexi-
 340 glass sheet was heated and pushed against a mould with the
 341 desired shape, then the bottom of the obtained object was cut
 342 to permit the free passage of light. The cylindrical section was
 343 obtained by cutting a plexiglass tube. The two sections were
 344 then glued together before evaporating the reflective layer. For
 345 the PMTs, the Photonis XP4508B with quartz window were
 346 chosen. The photoelectron yield was greater than ≈ 10 within
 347 the kinematic region of the experiment, thereby yielding a
 348 high electron detection efficiency down to a scattering angle
 349 of about 6° . Signals from the new Cherenkov were built into
 350 the main electron trigger during EG4. Consequently only 1/6
 351 of the full azimuthal acceptance of CLAS was used to detect
 352 and identify forward-angle scattered electrons.

354 B. The Polarized Electron Beam

355 The polarized electron beam was produced by illuminating
 356 a strained GaAs photocathode with circularly polarized light.
 357

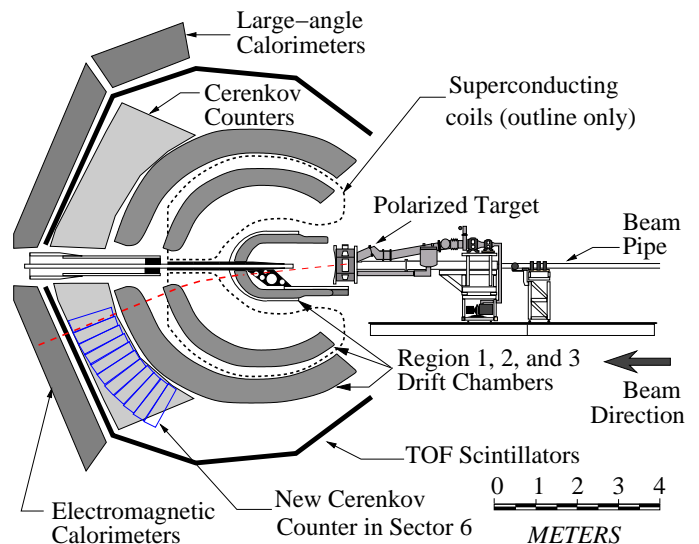


FIG. 2. (Color online) CLAS during EG4 showing the polarized target and the detector arrangement. A new Cherenkov detector consisting of 11 segments was installed in place of the original Cherenkov in sector 6. It provided the ability of detecting scattered electrons in the outbending configuration with scattering angles as small as 6° (dashed-line track).

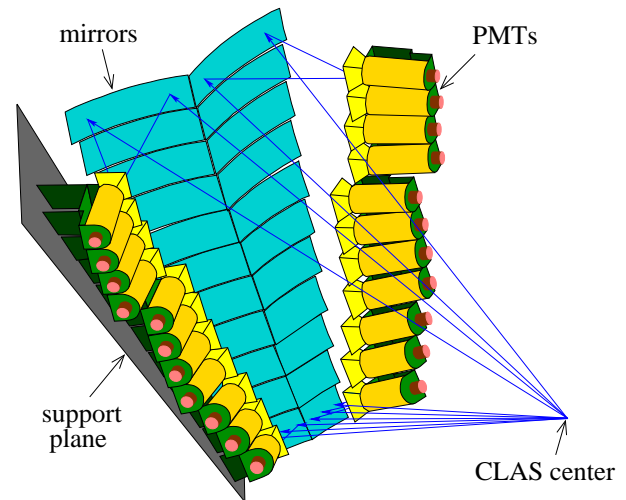


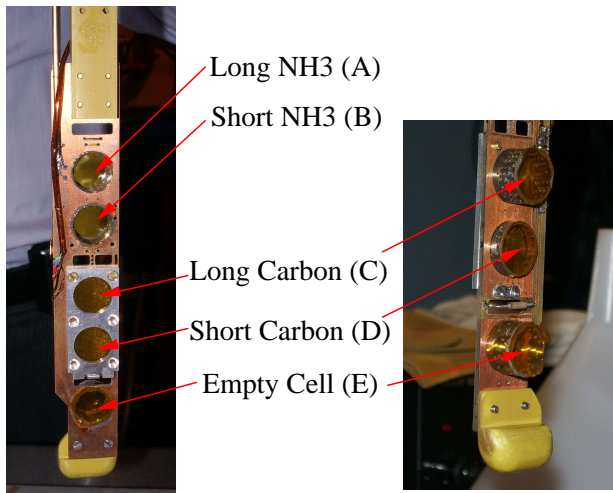
FIG. 3. (Color online) The new Cherenkov detector designed and built by the INFN-Genova group. It consists of 11 pairs of mirrors with spherical curvature, which reflect the Cherenkov light to corresponding photo-multiplier tubes (PMTs). Only one of the two support planes for the PMTs is shown here. The solid blue lines show simulated particle trajectories originated from the CLAS center and the reflection of the Cherenkov light towards the PMT.

357 The helicity of the electron beam was selected from a pseudo-
 358 random sequence, and followed a quartet structure of either
 359 “+ - - +” or “- + + -”, with each helicity state lasting 33 ms.
 360 The helicity sequence controlled the trigger system, and peri-
 361 ods of beam instability due to helicity reversal were rejected
 362 from the data stream. To reduce possible systematic uncer-
 363 tainties, data were taken for two different beam helicity con-

364 figurations, with the beam insertable half-wave plate (IHWP)
 365 inserted (in) and removed (out), respectively. The polarization
 366 of the electron beam was measured by both a Møller and
 367 a Mott polarimeter.

368 C. The Polarized Targets

369 The polarized targets used for EG4 were the frozen $^{15}\text{NH}_3$
 370 and $^{14}\text{ND}_3$ targets dynamically polarized at 1 K with a 5-
 371 Tesla field. These were the same as the targets used for pre-
 372 vious CLAS double-polarization measurements [39]. The tar-
 373 get material was irradiated with 20 MeV electrons prior to the
 374 experiment to impart the paramagnetic radicals necessary for
 375 dynamic polarization. It was subsequently stored in liquid ni-
 376 trogen (LN_2) until needed for the experiment. The material,
 377 in the form of 1-2 mm sized granules, was then removed from
 378 the LN_2 storage dewars and loaded into two cylindrical con-
 379 tainers on the target insert. The structure of the target insert is
 380 shown in Fig. 4. The containers were either 1.0 cm or 0.5 cm
 381 in length, hereafter referred to as the long and short cells, re-
 382 spectively. The insert was then quickly placed into the target
 383 “banjo”, a 1-2 liter vessel of 1-K liquid helium at the center of
 384 a 5-T superconducting split coil magnet. A complete descrip-
 385 tion of the polarized target can be found in Ref. [40].



386 FIG. 4. (Color online) Target insert used during the EG4 experiment. A 1.0-cm long NH_3 and the 0.5-cm long NH_3 targets were installed in the Long and Short NH_3 positions during the first half of the NH_3 run period. They were called the “long NH_3 top” and the “short NH_3 ” targets, respectively. During the second half of the NH_3 run, two 1.0-cm long NH_3 targets were installed in the Long and the Short positions; they were called the “long NH_3 top” and the “long NH_3 bottom” targets, respectively. For the ND_3 run period only one 1.0-cm long ND_3 target was installed in the Short position. The five target positions are labeled A, B, C, D, and E, as shown.

387 Due to the presence of gaps between the frozen crystals
 388 inside the target cell, even if the length of the target cell or
 389 the banjo could be determined precisely, the exact amount of
 390 polarized materials interacting with the electron beam could
 391

TABLE I. Targets used during EG4 along with their target lengths and densities. The target ID was the value recorded in the data. ID 10 was not used. The target position refers to the physical location on the target insert defined in Fig. 4.

Target ID	Target type	Target position	length (cm)	Density (g/cm^3)
1	long NH_3 top	A	1.0	0.917^a
2	long ND_3	B	1.0	1.056^a
3	empty cell with helium	E	1.0	0.145^b
4	long carbon	C	1.0, 0.216 ^c	2.166^d
5	short NH_3	B	0.5	0.917^a
6	short carbon	D	0.5, 0.108 ^c	2.166^d
7	long carbon no helium	C	1.0, 0.216 ^c	2.166^d
8	empty cell without helium	E	1.0	
9	short carbon without helium	D	0.5	2.166^c
11	long NH_3 bottom	B	1.0	0.917^a

^a For polarized NH_3 or ND_3 the densities are the density of the frozen polarized material beads.

^b Helium density.

^c The first and the second length values correspond to the cell length and the carbon foil thickness, respectively.

^d Carbon density.

392 not be directly measured. The fraction of the target filled by
 393 frozen polarized material is called the “packing factor” and is
 394 typically extracted by comparing the yield from the polarized
 395 target to those from carbon and “empty” targets. For the car-
 396 bon target, a carbon foil with known thickness was placed in
 397 an empty target cell and filled with liquid ^4He . There were two
 398 carbon targets, labeled “long” and “short” carbon, of which
 399 both the cell length and the foil thickness match those of the
 400 long and the short NH_3 targets, respectively. Empty targets
 401 refer to target cells with no solid material inside. Empty tar-
 402 gets can either be filled with liquid ^4He , or the ^4He can be
 403 completely pumped out. There was only one empty cell dur-
 404 ing EG4 to physically host the empty targets, which was 1.0
 405 cm in length.

406 During EG4 the polarized target was placed 1.01 m up-
 407 stream from the CLAS center to increase the acceptance at
 408 low Q^2 by reducing the minimum angle for the scattered elec-
 409 trons. The following targets were used: two 1.0-cm long and
 410 one 0.5-cm long NH_3 target, one 1.0-cm long ND_3 target, one
 411 0.216-cm and one 0.108-cm thick ^{12}C target, and one empty
 412 target. The target types during EG4 are defined in Table I. Un-
 413 less specified otherwise, “empty target” refers to target type 3
 414 [empty cell with helium (1 cm)] hereafter.

415 An NMR system was used to monitor the polarization of
 416 the target during the experiment, but was subject to three sys-
 417 tematic uncertainties that limited its suitability for data anal-
 418 ysis. First, the NMR coils were wrapped around the outside
 419 of the 1.5-cm diameter target cells, while the electron beam
 420 was only rastered over the central 1.2 cm portion of the target.
 421 The NMR signal was thus dominated by the material at the
 422

423 edges of the cell, and lacked sensitivity to the beam-induced
 424 depolarization of the material at the center. This uncertainty is
 425 difficult to estimate, as the effect depends on the accumulated
 426 dose. Second, for the EG4 experiment the two polarized target
 427 cells were adjacent to one another on the insert, as shown in
 428 Fig. 4, and cross-talk was observed between the cells' NMR
 429 circuits. Tests performed at the end of the experiment indi-
 430 cate that cross-talk could contribute an uncertainty of about
 431 5-10% to the polarization measurement due to its effect on
 432 the thermal-equilibrium calibration of the NMR signal. Third,
 433 calibration of the NMR system itself is normally subject to
 434 a 4-5% uncertainty. These three effects added up to a large
 435 systematic uncertainty to the target polarization measured by
 436 NMR. Therefore, it was decided that the asymmetries of ep
 437 elastic scattering would be used to extract the product of the
 438 beam and target polarizations $P_b P_t$ needed for the exclusive
 439 channel analysis reported here. The methods and results for
 440 the elastic $P_b P_t$ extraction will be described in Section III D.
 441 For NH_3 , the use of ^{15}N has the advantage that only one un-
 442 paired proton can be polarized, while all neutrons are paired
 443 to spin zero. The polarized proton in the ^{15}N does however af-
 444 fect the measured asymmetry by a small amount, as discussed
 445 in Section III G.

446 III. DATA ANALYSIS

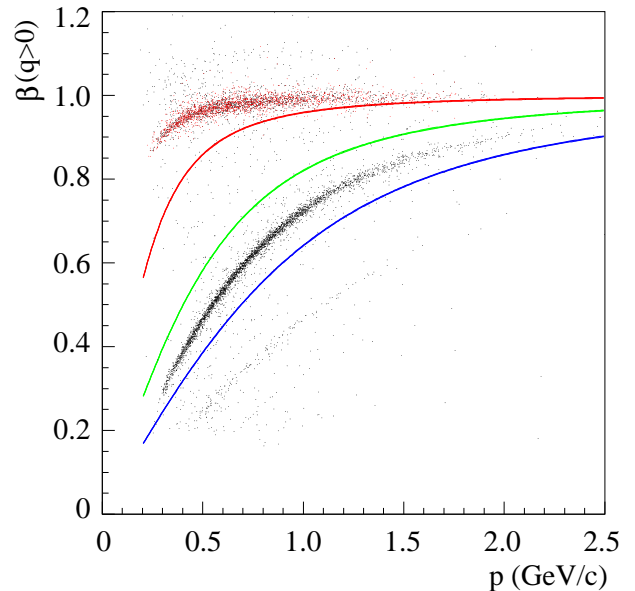
447 A. Exclusive Event Selection

448 Exclusive events $\vec{e}\vec{p} \rightarrow e'\pi^+(n)$ were identified by detect-
 449 ing the final state electron in coincidence with a pion and us-
 450 ing a missing mass cut to select the undetected neutron. For
 451 each event, we required that two particles be detected with
 452 the correct charges (-1 for the electron and $+1$ for the π^+).
 453 Each particle was required to have valid information from
 454 DC and TOF, and have reconstructed momentum greater than
 455 $0.3 \text{ GeV}/c$ ($0.1 \text{ GeV}/c$ higher than the momentum acceptance
 456 of CLAS [36]).

457 For particle identification, EC and CC signals were used
 458 to identify electrons. Cuts were applied on the EC: $E_{tot} >$
 459 $(p - 0.3) \times 0.22$, $E_{in} > (0.14p - 0.8E_{out})$ and $E_{in} > 0.035p$,
 460 where E_{in} and E_{out} are the energy deposited in the inner and
 461 the outer layers of the EC, respectively; $E_{tot} = E_{in} + E_{out}$
 462 and p is the particle momentum in GeV/c . These cuts were
 463 selected to optimize the separation of electrons (that pro-
 464 duce electromagnetic showers) from pions (that deposit en-
 465 ergy mostly through ionizations). We also required there to
 466 be only one hit in the CC, with its signal consistent with those
 467 from the EC and the TOF in both hit position and timing.

468 Pions were determined from a mass cut of $0.01 < m <$
 469 $0.30 \text{ GeV}/c^2$ and a TOF cut $|t_{TOF} - t_{\text{expected}}^\pi| < 1.0 \text{ ns}$.
 470 The expected flight time of the pion, t_{expected}^π , was calculated
 471 from the particle's momentum in combination with the timing
 472 of the electron. Figure 5 shows the effect of the TOF cut on
 473 the $\beta \equiv v/c$ vs. momentum p distributions, where v is the
 474 velocity amplitude (speed) of the particle. The TOF cut used
 475 clearly selected pions out of other particle background.

476 For each event, a vertex z was used. Here z is defined as



477 FIG. 5. β vs. p for all positively charged particles, with (red) and
 478 without (black) TOF cut for pions. The red, green and blue curves
 479 correspond to reconstructed masses of 0.3 , 0.7 and $1.2 \text{ GeV}/c^2$, re-
 480 spectively, which are typical cut-off values used to distinguish be-
 481 tween pions and kaons, kaons and protons, and protons and heavier
 particles. As can be seen, the positively charged particles detected
 consist of significant fractions of protons and heavier particles and a
 small fraction of kaons, but the $\pm 1.0 \text{ ns}$ TOF cut is quite effective
 in selecting pions. These data were collected on the long top NH_3
 target during the 3 GeV run period.

477 pointing along the beam direction with the origin coincides
 478 with the CLAS center. The polarized target was positioned
 479 upstream of the CLAS center during EG4 (see Fig. 2), and the
 480 center of the target was determined from empty target data to
 481 be at $z = -101 \text{ cm}$. The z cut was optimized to be

$$-106 \text{ cm} < z < -96 \text{ cm}, \quad (22)$$

483 where the range was determined using empty target data to
 484 exclude as much material outside the target as possible. See
 485 Fig. 7 in Section III C for a detailed presentation of the vertex
 486 z distribution.

487 Acceptance cuts, also called “fiducial cuts”, were applied
 488 on both electrons and pions using reconstructed DC variables.
 489 These acceptance cuts exclude regions where the detector ef-
 490 ficiency is not well understood, which often happens on the
 491 edge of the detectors, but could also include regions where
 492 certain parts of the detectors malfunctioned. Moreover, be-
 493 cause the main purpose of EG4 was measurement of the GDH
 494 sum, which only requires detection of inclusively-scattered
 495 electrons, not all six DC sectors were turned on during the
 496 run. This caused a variation in the ϕ^* acceptance of the exclu-
 497 sive channel. Determination of the acceptance and its effects
 498 on the asymmetries will be described in Sec. III H.

B. Beam Properties

499

As described in the previous section, the helicity of the electron beam followed a quartet structure. For EG4, the beam helicity of each event was delayed by 8 pulses (2 quartets) and then recorded in the data stream. This delayed recording helped to avoid cross-talk between the helicity signal and the electronics or data acquisition system in the hall. In the data analysis, the delay of the helicity sequence was corrected to match each event to its true beam helicity state. During this process, events with inconsistent recording of the helicity sequence were rejected.

A helicity dependence of the integrated beam charge causes a first-order correction to the measured physics asymmetry, and thus it is desired to keep the charge asymmetry as small as possible. The beam charge asymmetry was calculated using the charge measured by the Faraday cup. It was found to be below the percent level throughout the EG4 experiment, and for most runs had stable values at or below the 10^{-3} level.

Different methods for deriving the beam energy were used during EG4. The exact energies were 1.054, 1.338, 1.989, 2.260 and 2.999 GeV. The beam polarization was determined using a Møller polarimeter [36] in Hall B that measured the asymmetry in elastic electron-electron scattering. The results are shown in Fig. 6. Typically, Møller measurements were performed as soon as a change to the beam configuration was made, and then intermittently throughout the run period. Therefore, the beam polarization from each Møller measurement was applied retroactively to runs that immediately follow such configuration changes, and to runs that follow the Møller measurement until the next valid measurement is available. Two additional measurements were done using a Mott polarimeter [41–44], which is located near the injector where the beam electrons have reached 5 MeV in energy but before entering the first linac. The Mott polarimeter results were consistent with those from Møller measurements. The absolute beam helicity was determined using the $\sin \phi^*$ -weighted moment of the beam asymmetry A_{LU} in the $\Delta(1232)3/2^+$ region and comparing with results from previous experiments [45, 46]. Using the A_{LU} method, it was determined that when the beam IHWP is inserted, for beam energies 1.3 and 2.3 GeV, the positive DAQ helicity corresponds to the true negative helicity of the beam electron, while for other energies the positive DAQ helicity corresponds to the true positive electron helicity. These results are consistent with the sign change of the beam polarization measured with the Møller polarimeter.

C. Kinematic Corrections

Various corrections were applied to the kinematic variables reconstructed from the detectors [47]. The first is the raster correction: in order to avoid the electron beam overheating the target, the beam was rastered in a circular pattern during EG4 using four magnets located upstream of the target. The values of the magnet current were recorded in the data stream and were used to calculate the beam position (x, y) at the target.

EG4 Moeller Polarization

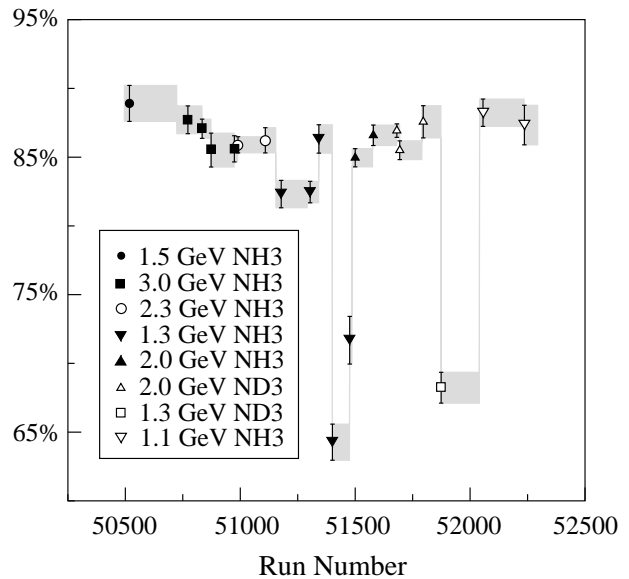


FIG. 6. Beam polarization from Møller measurements vs. run number for the whole EG4 experiment. The grey bands represent extrapolations of the beam polarization to the corresponding range of runs as described in the text.

The beam position was then used to re-calculate the vertex position along the beam direction z . After the raster correction was applied, the average value of the z positions of all particles in the same event was taken as the true vertex position of the event, see Fig. 7 [47]. The polar and the azimuthal angles θ and ϕ of each particle were also corrected using the new beam and vertex positions. This procedure took into account the multiple scattering effect that affected the reconstructed vertex position randomly for each particle.

Due to uncertainties in our knowledge of the drift chamber positions and of the shape and location of the torus coils, a systematic shift of the particle momentum was present. To correct for this shift, the magnitude of the reconstructed particle momentum p and the polar angle θ were adjusted using sector-dependent parameters. The detailed method for the momentum correction is described in Ref. [48] and results for this experiment are given in Ref. [47]. For sector 6 equipped with the new Cherenkov counter, inclusive elastic ep scattering events were used to optimize the correction based on the invariant mass W position of the elastic peak. For the other sectors, electron triggers were not available and hadrons from exclusive events such as $ep \rightarrow e'p'X$, $ep \rightarrow e'\pi^+\pi^-X$, and exclusive events $ep \rightarrow e'p'\pi^+\pi^-$ were used to optimize the corrections.

Finally, the momentum of each particle was corrected for the energy loss due to passage through material enclosed in the target banjo and the target windows. For electrons a single value $dE/dx = 2.8 \text{ MeV}/(\text{g}/\text{cm}^2)$ was used, while for other particles the Bethe-Bloch equation [49] was used to calculate the ionization loss.

Figure 8 shows the effect on the missing mass spectrum for

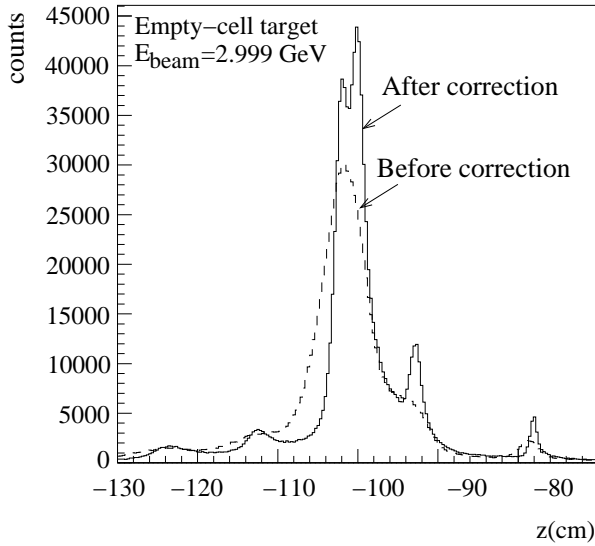


FIG. 7. Electrons' vertex z position before (dashed) and after (solid) raster corrections, taken with the empty target with the 3 GeV beam. While the beam line exit window (at $z = -78.3$ cm) can be seen both before and after the correction, the banjo windows (at $z = -100$ and -102 cm), the 4 K heat shield ($14 \mu\text{m}$ aluminum at $z = -121.0$ cm), some target structure at $z \approx -112$ cm, and several insulating foils (aluminum or aluminized mylar, between $z = -90.5$ and -94.1 cm), become visible only after the raster correction. The vertex z cut, Eq. (22), corresponds to slightly more than 3σ in the target thickness [47].

584 the $ep \rightarrow e'\pi^+(X)$ channel from kinematic corrections.

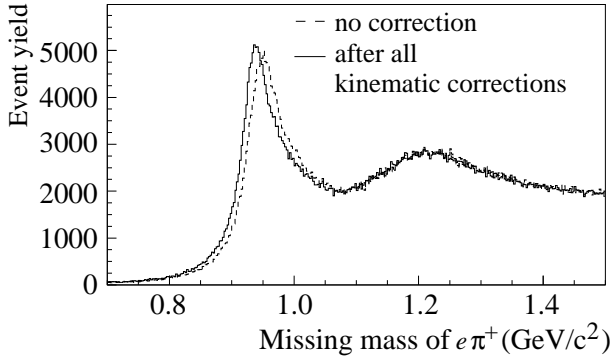


FIG. 8. Missing mass spectrum for the $e + p \rightarrow e'\pi^+(X)$ channel before (dashed) and after all kinematics corrections (solid), from six 3.0-GeV long top NH_3 target runs. After all corrections, the peak center is closer to the expected value (the neutron mass).

D. Elastic Scattering for Extracting $P_b P_t$

588 The product of the beam and the target polarizations $P_b P_t$
589 is needed to directly correct the exclusive channel asymme-
590 tries. During EG4, the target polarization P_t was measured by

591 NMR and the beam polarization P_b by the Møller polarimetry.
592 However, due to reasons described in Section II C, the NMR
593 measurements had large uncertainties and an alternate method
594 had to be used. For EG4 we extracted $P_b P_t$ for all beam en-
595 ergies by comparing the double spin asymmetry of elastic ep
596 events to the expected value:

$$P_b P_t = \frac{A_{\text{meas}}^{el}}{A_{\text{th}}^{el}}, \quad (23)$$

598 where the measured elastic asymmetry was extracted from
599 data using

$$A_{\text{meas}}^{el} = \frac{A_{\text{raw}}^{el}}{f_{el}}, \quad (24)$$

601 with f_{el} the elastic dilution factor to account for the effect of
602 events scattered from unpolarized material in the target. The
603 raw asymmetry was evaluated as

$$A_{\text{raw}}^{el} = \frac{\frac{N_R^{el}}{Q_R} - \frac{N_L^{el}}{Q_L}}{\frac{N_R^{el}}{Q_R} + \frac{N_L^{el}}{Q_L}}, \quad (25)$$

604 where $N_{R(L)}^{el}$ and $Q_{R(L)}$ are the elastic event yield and the
605 beam charge for the right- (left-)handed beam electrons, re-
606 spectively. The expected elastic-scattering asymmetry A_{th}^{el}
607 was calculated using

$$A_{\text{th}}^{el} = -2\sqrt{\frac{\tau}{1+\tau}} \tan \frac{\theta_e}{2} \times \frac{\left[\sqrt{\tau(1+(1+\tau)\tan^2 \frac{\theta_e}{2})} \cos \theta_e + \sin \theta_e \frac{G_E^p}{G_M^p} \right]}{\left[\frac{(G_E^p/G_M^p)^2 + \tau}{1+\tau} + 2\tau \tan^2 \frac{\theta_e}{2} \right]} \quad (26)$$

611 with $\tau = Q^2/(4M^2)$. The proton form factor fits from
612 Ref. [50] were used:

$$G_E^p = 1/[1 + 0.62Q + 0.68Q^2 + 2.8Q^3 + 0.83Q^4] \quad (27)$$

614 and

$$G_M^p = 2.79/[1 + 0.35Q + 2.44Q^2 + 0.5Q^3 + 1.04Q^4 + 0.34Q^5] \quad (28)$$

617 with $Q \equiv \sqrt{Q^2}$ in GeV/c . Using a more updated fit of the
618 proton form factors than Ref. [50] would change the asymme-
619 try value by less than 2% relative.

620 Elastic events were identified using two methods: 1) in-
621 clusive elastic events where only the scattered electron was
622 detected and a cut on the invariant mass W near the proton
623 peak was applied; and 2) exclusive elastic events where
624 both the scattered proton and electron were detected and cuts
625 were applied to the electron and the proton azimuthal angles:
626 $|\phi_e - \phi_p - 180^\circ| < 3^\circ$, the polar angles of the proton and
627 the electron's momentum transfer \vec{q} : $|\theta_p - \theta_q| < 2^\circ$, and the
628 missing energy $E_{\text{miss}} < 0.15$ GeV. The exclusive analysis
629 had limited statistics and only worked for the 3.0 and the 2.3
630 GeV data sets. For lower beam energies, the proton's scatter-
631 ing angle was typically greater than 49° , and was blocked by

632 the polarized target coils. Therefore the $P_b P_t$ value extracted
633 from exclusive elastic events was only used as a cross-check
634 of the $P_b P_t$ from inclusive events.

635 The presence of unpolarized material reduces the measured
636 asymmetry, and this effect is described as a dilution factor
637 in the analysis. The dilution factor for the inclusive elastic
638 events, f_{el}^{incl} , was extracted by comparing the invariant mass
639 W spectrum of the polarized target to that computed for the
640 unpolarized material. The beam-charge-normalized W spec-
641 trum for the unpolarized material in the polarized target, de-
642 noted as $\frac{N_N \text{ in } NH_3}{Q_{NH_3}}$, was calculated using the spectra of the
643 carbon and the empty target, the known thickness and density
644 of the carbon and the empty target, and the polarized target's
645 packing factor x_{NH_3} defined as the absolute length of the po-
646 larized material in the polarized target:

$$647 \quad \frac{N_N \text{ in } NH_3}{Q_{NH_3}} = r_C \frac{N_{12C}}{Q_{12C}} + r_{empt} \frac{N_{empt}}{Q_{empt}}, \quad (29)$$

648 where $N_{12C(empt)}$ and $Q_{12C(empt)}$ are the yield and the beam
649 charge of the carbon (empty) target data. The scaling factors
650 are

$$651 \quad r_C = \frac{(B_{NH_3} \rho_{NH_3} x_{NH_3} + B_w \rho_w x_w \frac{x_{NH_3}}{l})}{B_{12C} \rho_{12C} x_{12C} + B_w \rho_w x_w \frac{x_{12C}}{l}}, \quad (30)$$

$$652 \quad r_{empt} = \left(1 - \frac{x_{NH_3}}{l}\right) - \left(1 - \frac{x_{12C}}{l}\right) r_C, \quad (31)$$

653 where x_{12C} is the thickness of the carbon foil in the carbon tar-
654 get, x_w is the sum of thicknesses of other unpolarized material
655 in the target, l is the target banjo length (1.0 cm for the long
656 target and 0.5 cm for the short target), and $B_{12C,w} = 1$ are the
657 bound-nucleon fractions of the carbon target and other unpo-
658 larized material in the target, respectively. The values of x for
659 the various materials are given in Table II. The bound-nucleon
660 fraction for the NH_3 target takes into account both the fraction
661 of bound nucleons and a correction for the extra neutron in the
662 ^{15}N : $B_{NH_3} = (14 + \sigma_n / \sigma_N) / 18$ with $\sigma_N = (\sigma_p + \sigma_n) / 2$ and
663 $\sigma_{p,n}$ are the calculated elastic cross sections for the proton and
664 the neutron, respectively.

665 After the contribution from the unpolarized material was
666 known, the dilution factor was calculated using

$$667 \quad f_{el}^{incl} = \frac{N_p \text{ in } NH_3}{N_{NH_3}} = \frac{N_{NH_3} - N_N \text{ in } NH_3}{N_{NH_3}}, \quad (32)$$

668 where N_{NH_3} is the total number of events from the NH_3 tar-
669 get. The dilution correction to the elastic asymmetry was then
670 applied using Eq. (24). In the present analysis, elastic events
671 below $Q^2 = 0.156 \text{ (GeV}/c)^2$ could not be used because of
672 electrons scattered elastically from nuclei in the target, such
673 as 4He and nitrogen. These low Q^2 bins were rejected in the
674 $P_b P_t$ analysis.

675 Figure 9 shows the W spectrum decomposition for 1.1 and
676 3.0 GeV inclusive elastic scattering data for two Q^2 bins. The
677 low Q^2 bin (top) is to illustrate the effect of the nuclear elastic
678 scattering and these bins were rejected from the $P_b P_t$ analysis.
679 The high Q^2 bin (bottom) shows no such effect and the $P_b P_t$
680 extracted are considered reliable. After the $P_b P_t$ value was
681 extracted for individual Q^2 bins, the results were checked to

TABLE II. Material used for the EG4 target and their locations in
increasing order of z , in the range $z = (-120, -80)$ cm. The ra-
tios Z/A were used in the dilution factor analysis of the exclusive
channel, see Sec.III F.

location z (cm)	Material	Density (g/cm ³)	Thickness	Z/A
-101.9	banjo entrance window, Al	2.7	71 μm	13./26.982
varies	target entrance window, kapton	1.42	25 μm	0.51264
varies	NH_3	0.917	x^a	7/18
varies	long ^{12}C	2.166	$2.16 \pm 0.05 \text{ mm}$	6/12
varies	liquid 4He	0.145	$l - x^a$	2/4
varies	target entrance window kapton	1.42	25 μm	0.51264
-99.6	banjo exit win- dow Al	2.7	71 μm	13./26.982

^a l is the banjo length and x is either the packing factor (for NH_3
targets) or the carbon foil thickness (for carbon targets).

682 ensure there was no systematic Q^2 -dependence, which would
683 imply a problem with the analysis. The $P_b P_t$ results were then
684 averaged over all Q^2 bins above $0.156 \text{ (GeV}/c)^2$. This was
685 done for each individual run and the run-by-run, Q^2 -averaged
686 $P_b P_t$ results were used to correct the asymmetries from the
687 exclusive channel. Figure 10 illustrates the variation of $P_b P_t$
688 during the experiment.

689 The uncertainty of the packing factor x_{NH_3} used in the
690 analysis was checked using the W spectrum below $W =$
691 $0.9 \text{ (GeV}/c)^2$, since an incorrect normalization would yield
692 an over- or an under-subtraction of the yield from unpolarized
693 material. For the 2.3 and 3.0 GeV data the value of x_{NH_3} was
694 confirmed by comparing the $P_b P_t$ value extracted from the
695 inclusive to that from the exclusive elastic events. The pack-
696 ing factor and its uncertainty also affect the dilution analysis
697 of the exclusive channel, to be described in the next sections,
698 thus the final results on $P_b P_t$ for each combination of beam
699 energy and polarized target type are shown together with the
700 exclusive channel dilution results in Table III. The relatively
701 larger error bar for the 1.1 GeV NH_3 long bottom target is
702 because most of the data were affected by the nuclear elastic
703 scattering and there are very limited Q^2 bins available for the
704 elastic $P_b P_t$ analysis.

705 In addition to checking the W spectrum and the com-
706 parison between inclusive and exclusive elastic events, the
707 $en \rightarrow e' \pi^- (p)$ channel was also used to check x_{NH_3} because
708 these events come primarily from the unpolarized neutrons of
709 the nitrogen in the target and thus should have a dilution fac-
710 tor of zero. The $e' \pi^- (p)$ events were analyzed for all beam
711 energies and it was found the dilution factors calculated using
712 the x_{NH_3} values in Table III were indeed consistent with zero.
713 As a last check, the run-by-run values of $P_b P_t$ were compared
714 with the numerous target material and configuration changes
715 during the experiment, and were found to be consistent with
716 the physical changes of the target.

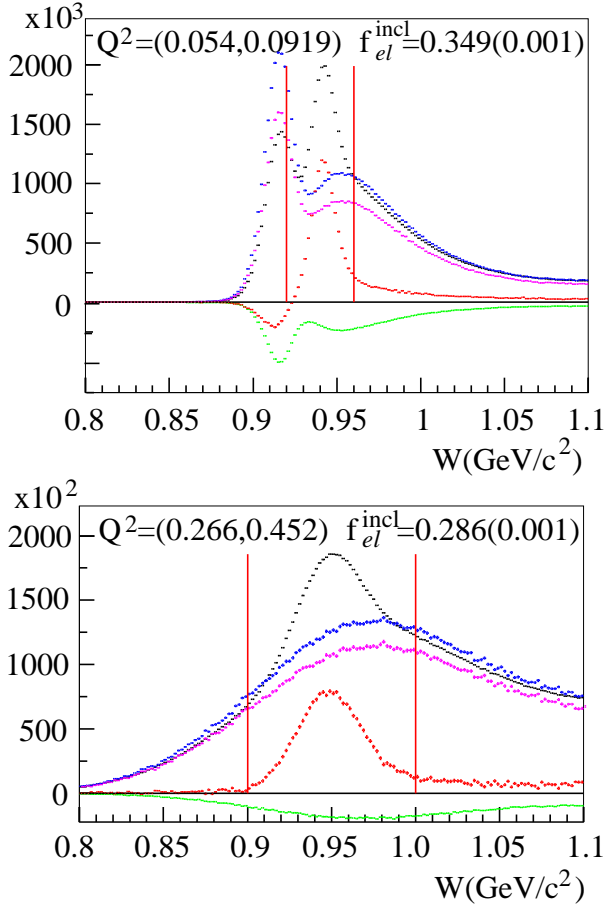


FIG. 9. W -spectrum for dilution calculation for inclusive elastic $P_b P_t$ analysis. Top: 1.1 GeV data on NH_3 long bottom target in the $Q^2 = (0.054, 0.092)$ $(\text{GeV}/c)^2$ bin; bottom: 3.0 GeV data on NH_3 long top target in the $Q^2 = (0.266, 0.452)$ $(\text{GeV}/c)^2$ bin. For each panel, histograms from the carbon target (blue) and empty target (green) were scaled using Eqs. (30-31) using a packing factor of 0.75 cm for 1.1 GeV and 0.65 cm for 3.0 GeV respectively, and their sum gave the estimated contribution from unpolarized material in the NH_3 target (magenta). This unpolarized background was then subtracted from the NH_3 spectrum (black) to estimate the contribution from polarized protons in the target (red). The calculated elastic dilution factors are shown for each set of data with their uncertainties in the brackets. The W cuts used to select elastic events are shown as the two red vertical lines. Note that the scaled empty target spectrum (green) is negative, indicating that for the chosen packing factor we have scaled up the carbon data and then subtracted the extra helium to reproduce the unpolarized background in NH_3 . For Q^2 bins below 0.156 $(\text{GeV}/c)^2$, the nuclear elastic event contaminates the ep elastic peak and the extraction of the dilution factor is not reliable. For this reason, data with $Q^2 < 0.156$ $(\text{GeV}/c)^2$ were rejected from the elastic $P_b P_t$ analysis.

717 E. Extraction of Exclusive Channel Asymmetries

718 To extract the exclusive channel asymmetries, the $e'\pi^+(n)$
 719 channel events were divided into four-dimensional bins in W ,
 720 Q^2 , $\cos\theta^*$ and ϕ^* and then the asymmetries were extracted
 721 from the counts in each bin. The event counts for the four

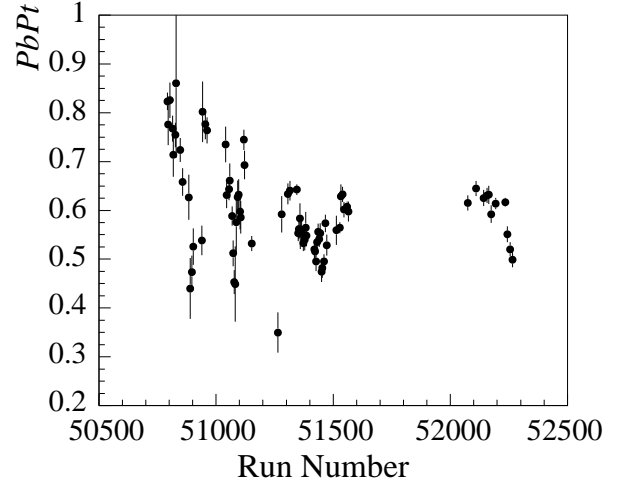


FIG. 10. Magnitude of $P_b P_t$ extracted from inclusive elastic scattering events for all runs used in the present analysis that were taken on the polarized NH_3 target. For illustration purposes, results from adjacent runs that shared the same beam insertable half-wave plate status were combined and are shown as one data point here. The error bars shown are statistical uncertainties determined by the number of available elastic events.

722 combinations of beam helicities and target polarization can be
 723 written, based on Eq. (5), as

$$724 \quad N_{\uparrow\uparrow} = D_1 \left[\sigma_0 + P_b^\uparrow \sigma_e + f_{\text{dil}}^\pi P_t^\uparrow \sigma_t + P_b^\uparrow f_{\text{dil}}^\pi P_t^\uparrow \sigma_{et} \right] \quad (33)$$

$$725 \quad N_{\downarrow\downarrow} = D_2 \left[\sigma_0 - P_b^\uparrow \sigma_e + f_{\text{dil}}^\pi P_t^\uparrow \sigma_t - P_b^\uparrow f_{\text{dil}}^\pi P_t^\uparrow \sigma_{et} \right] \quad (34)$$

$$726 \quad N_{\uparrow\downarrow} = D_3 \left[\sigma_0 + P_b^\downarrow \sigma_e - f_{\text{dil}}^\pi P_t^\downarrow \sigma_t - P_b^\downarrow f_{\text{dil}}^\pi P_t^\downarrow \sigma_{et} \right] \quad (35)$$

$$727 \quad N_{\downarrow\uparrow} = D_4 \left[\sigma_0 - P_b^\downarrow \sigma_e - f_{\text{dil}}^\pi P_t^\downarrow \sigma_t + P_b^\downarrow f_{\text{dil}}^\pi P_t^\downarrow \sigma_{et} \right] \quad (36)$$

728 where the arrows in the subscripts of N are for the beam he-
 729 licities (\uparrow or \downarrow) and the target spin directions (\uparrow or \downarrow), respec-
 730 tively, with \uparrow and \uparrow being positive helicity or parallel to the
 731 beam direction and \downarrow and \downarrow being negative helicity or anti-
 732 parallel to the beam direction. The parameters P_b^\uparrow and P_b^\downarrow are
 733 the statistically-averaged target or beam polarizations when
 734 the target spin is aligned and anti-aligned to the beamline, re-
 735 spectively. The dilution factor f_{dil}^π for the exclusive channel
 736 $\vec{e}\vec{p} \rightarrow e'\pi^+(n)$ is defined as the fractional yield from the po-
 737 larized proton in the NH_3 target, which effectively changes
 738 the target polarization. The four parameters $D_{1,2,3,4}$, relating
 739 event counts to cross sections, are related to the total beam
 740 charge, target thickness, spectrometer acceptance, and detec-
 741 tor efficiencies for each configuration. For stable running pe-
 742 riods with no significant change in the target cell, the spec-
 743 trometer setting and the detector status, the D factor is strictly
 744 proportional to the accumulated beam charge in each setting.
 745 From Eqs. (33–36), one can form the asymmetries as:

$$746 \quad A_{LU} = \frac{1}{P_b^\uparrow P_b^\downarrow} \times$$

$$\left[\frac{\left(\frac{N_{\uparrow\downarrow}}{D_3} - \frac{N_{\downarrow\downarrow}}{D_4} \right) P_b^\uparrow P_t^\uparrow + \left(\frac{N_{\uparrow\uparrow}}{D_1} - \frac{N_{\downarrow\uparrow}}{D_2} \right) P_b^\downarrow P_t^\downarrow}{\left(\frac{N_{\uparrow\uparrow}}{D_1} + \frac{N_{\downarrow\uparrow}}{D_2} \right) P_t^\downarrow + \left(\frac{N_{\uparrow\downarrow}}{D_3} + \frac{N_{\downarrow\downarrow}}{D_4} \right) P_t^\uparrow} \right], \quad (37)$$

$$A_{UL} = \frac{1}{f_{\text{dil}}^\pi} \frac{\left(\frac{N_{\uparrow\uparrow}}{D_1} + \frac{N_{\downarrow\uparrow}}{D_2} \right) - \left(\frac{N_{\uparrow\downarrow}}{D_3} + \frac{N_{\downarrow\downarrow}}{D_4} \right)}{\left(\frac{N_{\uparrow\uparrow}}{D_1} + \frac{N_{\downarrow\uparrow}}{D_2} \right) P_t^\downarrow + \left(\frac{N_{\uparrow\downarrow}}{D_3} + \frac{N_{\downarrow\downarrow}}{D_4} \right) P_t^\uparrow} \quad (38)$$

$$A_{LL} = \frac{1}{P_b^\uparrow P_b^\downarrow f_{\text{dil}}^\pi} \times \frac{\left[\left(\frac{N_{\uparrow\downarrow}}{D_3} - \frac{N_{\downarrow\downarrow}}{D_4} \right) P_b^\uparrow - \left(\frac{N_{\uparrow\uparrow}}{D_1} - \frac{N_{\downarrow\uparrow}}{D_2} \right) P_b^\downarrow \right]}{\left[\left(\frac{N_{\uparrow\uparrow}}{D_1} + \frac{N_{\downarrow\uparrow}}{D_2} \right) P_t^\downarrow + \left(\frac{N_{\uparrow\downarrow}}{D_3} + \frac{N_{\downarrow\downarrow}}{D_4} \right) P_t^\uparrow \right]}. \quad (39)$$

F. Dilution Factor for the Exclusive Channel

In contrast to the dilution for inclusive $P_b P_t$ analysis that has only Q^2 dependence (Section III D), the dilution for exclusive pion production could vary with all four kinematic variables W , Q^2 , $\cos\theta^*$ and ϕ^* [51]. To evaluate the dilution factor for all 4-dimensional bins of $(W, Q^2, \cos\theta^*, \phi^*)$, the yield from the unpolarized material inside the polarized NH_3 target was constructed using the missing mass spectra from the carbon and the empty targets. Scaling factors for the carbon and empty target data were calculated following a prescription similar to Eqs. (29-31), but with the bound-nucleon fraction B replaced by the ratio Z/A (Table II) for the $ep \rightarrow e'\pi^+(n)$ [$(1 - Z/A)$ for the $en \rightarrow e'\pi^-(p)$] channel. For NH_3 one should use $\frac{Z_{\text{NH}_3}}{A_{\text{NH}_3}} = 7/18$ to account for only unpolarized protons. We obtain:

$$\frac{N_N \text{ in } \text{NH}_3}{Q_{\text{NH}_3}} = a \left(\frac{N_{12\text{C}}}{Q_{12\text{C}}} \right) + b \left(\frac{N_{\text{empt}}}{Q_{\text{empt}}} \right), \quad (40)$$

where

$$a = \frac{\left(\frac{Z_{\text{NH}_3}}{A_{\text{NH}_3}} \rho_{\text{NH}_3} x_{\text{NH}_3} \right) + \left(\frac{Z_w}{A_w} \rho_w x_w \right) \frac{x_{\text{NH}_3}}{l}}{\left(\frac{Z_{12\text{C}}}{A_{12\text{C}}} \rho_{12\text{C}} x_{12\text{C}} \right) + \left(\frac{Z_w}{A_w} \rho_w x_w \right) \frac{x_{12\text{C}}}{l}}, \quad (41)$$

$$b = \left(1 - \frac{x_{\text{NH}_3}}{l} \right) - \left(1 - \frac{x_{12\text{C}}}{l} \right) a. \quad (42)$$

Similar to elastic analysis, the value of b from Eq. (42) could be either positive or negative depending on the input packing factor. Figure 11 shows the dilution factor evaluation for the 3.0 GeV data using the NH_3 long top target.

From Eqs. (38-39) one can see that the uncertainties in $P_b P_t$ and f_{dil}^π should be evaluated at the same time because both depend on the packing factor. Table III shows all $P_b P_t$ and dilution results for the packing factor range used in the elastic $P_b P_t$ analysis. For each setting of beam energy and target, we varied the packing factor by one standard deviation and evaluated $P_b P_t$ and $f_{\text{dil}}^{\pi^+}$. We used the observed difference in the product $P_b P_t f_{\text{dil}}^{\pi^+}$ as the uncertainty due to the packing factor, labeled as $P_b P_t f_{\text{dil}}^{\pi^+} \pm (p.f.)$. For the total uncertainty $\frac{\Delta(P_b P_t f_{\text{dil}})}{P_b P_t f_{\text{dil}}}$ (total), we added the following terms in quadrature: 1) statistical uncertainty of inclusive elastic events used

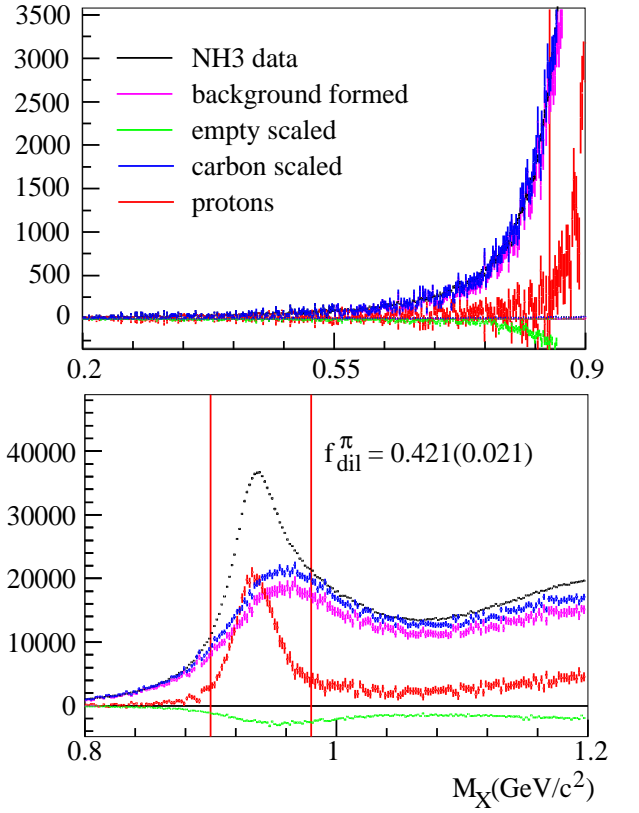


FIG. 11. Missing mass M_X spectrum for deriving the dilution factor for the $ep \rightarrow e'\pi^+(n)$ channel. Top: missing mass below the neutron mass peak; bottom: missing mass around the neutron mass peak. The data shown are for the 3.0 GeV run period using the NH_3 long top target. Here, the M_X spectrum for the nuclear material (magenta) in the polarized NH_3 target was constructed using the spectra for the carbon target (blue), the empty target (green), with an input packing factor $x = 0.65$ cm. The nuclear contribution was then subtracted from the NH_3 target spectrum (black) to give the polarized-proton spectrum (red). The dilution factor was evaluated using the region around the neutron peak and is shown in the bottom panel with the uncertainty in the bracket. The histogram and the dilution uncertainties include both statistical uncertainties and the uncertainty in the scaling or packing factors. Note that the empty target (green) spectrum is negative, indicating we have scaled up the carbon data and then subtracted the extra helium (empty target) to reproduce the unpolarized background in NH_3 . Results for the dilution factor is shown in the bottom plot. The M_X cuts (0.90, 0.98) GeV/c^2 used in the dilution and the asymmetry analysis are shown by the two red vertical lines.

in the $P_b P_t$ analysis; 2) statistical uncertainty of the carbon and empty target counts used to calculate the dilution factor for inclusive elastic events; 3) statistical uncertainty in the exclusive $ep \rightarrow e'\pi^+(n)$ channel due to limited statistics of carbon and empty target data $f_{\text{dil}}^{\pi^+} \pm (\text{stat.})$; and 4) the observed variation in $P_b P_t f_{\text{dil}}^{\pi^+}$ when the input packing factor was varied within its uncertainty. The resulting total uncertainties on $P_b P_t f_{\text{dil}}^{\pi^+}$ were used for the evaluation of the uncertainty of the double-spin asymmetry A_{LL} . For the target asymmetry

795 A_{UL} , the uncertainty was evaluated by combining the uncer-
 796 tainty of $P_b P_t f_{\text{dil}}^{\pi^+}$ and the uncertainty of the Møller measure-
 797 ments on the beam polarization. The uncertainty from the
 798 polarizations and the dilution is the largest systematic uncer-
 799 tainty of the present analysis.

800 The uncertainty in the input packing factor of Table III was
 801 checked using not only the W spectrum of elastic events (as
 802 described in Section III D), but also the dilution factor of the
 803 $en \rightarrow e'\pi^-(p)$ channel analyzed using a similar prescription
 804 as Eqs. (40-42). The dilution factor of the $\pi^-(p)$ channel
 805 should be consistent with zero in all kinematic bins. Over-
 806 all, the lower bound in the packing factor was cross-checked
 807 between the $en \rightarrow e'\pi^-(p)$ dilution result and the elastic W
 808 spectrum, and the upper bound in the packing factor was de-
 809 termined always by the elastic W spectrum.

810 The kinematics dependence of the dilution factor on Q^2 , W
 811 and the pion center-of-mass angles θ^* and ϕ^* have been stud-
 812 ied, and multi-dimensional fits of the dependence were per-
 813 formed. The limited statistics of the carbon and the empty tar-
 814 get data prevented fitting the $(Q^2, W, \cos\theta^*, \phi^*)$ dependence
 815 simultaneously. Instead, two bi-dimensional fits were used,
 816 one for the (Q^2, W) dependence and one for the $(\cos\theta^*, \phi^*)$
 817 dependence, with the following ad-hoc parameterizations:

$$818 \quad f_1 = p_0 \left[1 + p_1(Q^2) + p_2(Q^2)^2 \right] \\
 819 \quad \times \left[1 + p_3(W - 1.8) + p_4(W - 1.8)^2 \right] \\
 820 \quad \times \left[1 + \frac{p_5}{(W^2 - 1.50^2)^2 + 1.50^2 \times 0.05^2} \right] \\
 821 \quad \times \left[1 + \frac{p_6}{(W^2 - 1.68^2)^2 + 1.68^2 \times 0.05^2} \right] \quad (43)$$

822 where W is in GeV/c^2 and

$$823 \quad f_2 = p'_0 \times \left[1 + \frac{p_7}{1 - \cos\theta^*} \right] \\
 824 \quad \times [1 + p_8 \sin\phi^* + p_9 \cos\phi^*]. \quad (44)$$

825 The resulting two fits were then multiplied to give the over-
 826 all 2×2 -dimensional fit for $f_{\text{dil}}^{\pi^+}(W, Q^2, \cos\theta^*, \phi^*)$. To check
 827 the validity of the fit, the results from $f_{\text{dil}}^{\pi^+}(W, Q^2, \cos\theta^*, \phi^*)$
 828 were integrated over 3 of the 4 variables, and then com-
 829 pared with the dilution extracted directly from data binned
 830 in the 4th variable. This comparison is shown in Fig. 12.
 831 One can see that the dilution factors obtained from this
 832 method agree with data very well. The 2×2 -dimensional
 833 fit $f_{\text{dil}}^{\pi^+}(W, Q^2, \cos\theta^*, \phi^*)$ was used to correct the asymme-
 834 tries A_{UL} and A_{LL} for the specific $W, Q^2, \cos\theta^*, \phi^*$ bin us-
 835 ing Eqs. (38-39).

837 G. Effect of Nitrogen Polarization on the Asymmetry

838 The ^{15}N in the NH_3 target is polarizable and can affect the
 839 measured asymmetry. In this section we estimate this effect
 840 and show that it is negligible. Therefore no correction was
 841 made to the extracted exclusive channel asymmetries.

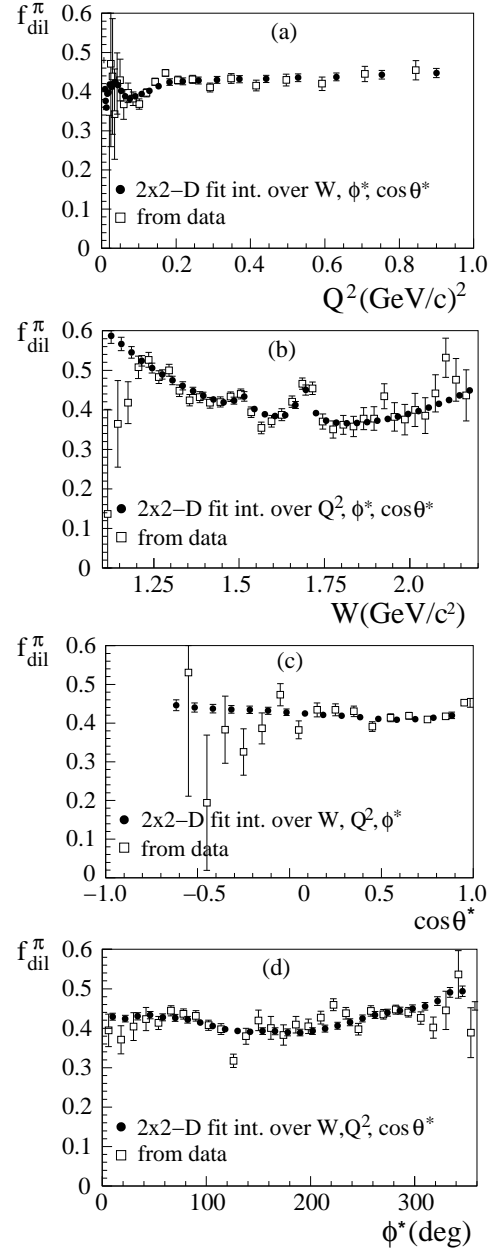


FIG. 12. Dependence of dilution on: (a) Q^2 , (b) W , (c) $\cos\theta^*$ and
 (d) ϕ^* , for the 3.0 GeV NH_3 long top target, $ep \rightarrow e'\pi^+(n)$ channel,
 obtained directly from the data (open squares) and from multiplying
 the two 2D fits of Eqs. (43-44) then integrating over 3 of the 4 vari-
 ables (solid circles). The error bars for the dilution extracted from
 data are statistical only.

842 The nitrogen polarization in $^{15}\text{NH}_3$ can be estimated based
 843 on the Equal Spin Temperature (EST) prediction [39]:

$$844 \quad P(^{15}\text{N}) = \tanh \frac{\mu_{^{15}\text{N}} B}{kT_S}, P(\text{H}) = \tanh \frac{\mu_p B}{kT_S}, \quad (45)$$

845 where $\mu_{^{15}\text{N}}$ and μ_p are the magnetic moments of the ^{15}N and
 846 the proton, respectively, B is the magnetic field of the target, k
 847 is the Boltzmann constant and T_S is the spin temperature that
 848 describes the Boltzmann distribution of spins inside the target.

TABLE III. Dilution factor $f_{\text{dil}}^{\pi^+}$ and the product $P_b P_t f_{\text{dil}}^{\pi^+}$ for the exclusive π^+ channel. The $P_b P_t$ results extracted from inclusive elastic scattering, described in section III D, and their uncertainties are also shown. For $P_b P_t$, the three errors are due to statistical uncertainty of the elastic events, the statistical uncertainty of the carbon and empty target counts used to calculate the dilution factor for inclusive elastic analysis, and the uncertainty of the packing factor. $P_b P_t$ values from Møller and NMR measurements are shown for comparison, although the NMR measurements are unreliable as described in section II C. The products $P_b P_t f_{\text{dil}}^{\pi^+}$ are used to correct the exclusive channel asymmetries. The total uncertainties in $P_b P_t f_{\text{dil}}^{\pi^+}$ include uncertainties of $P_b P_t$, statistical uncertainties of $f_{\text{dil}}^{\pi^+}$, and the uncertainties due to the packing factor (p.f.), all added in quadrature. These total uncertainties will be used as systematic uncertainties on the extracted exclusive channel asymmetries.

E_{beam} (GeV)	Target (NH ₃)	p.f. (cm)	$(P_b P_t)_{el}$	Møller \times NMR	$f_{\text{dil}}^{\pi^+} \pm (\text{stat.}) \pm (\text{p.f.})$	$P_b P_t f_{\text{dil}}^{\pi^+}$	$\frac{\Delta(P_b P_t f_{\text{dil}}^{\pi^+})}{P_b P_t f_{\text{dil}}^{\pi^+}}$ (total)
3.0	top	0.65 ± 0.05	$0.614 \pm 0.006 \pm 0.015 \pm 0.045$	0.620	$0.424 \pm 0.021 \pm 0.013$	0.260	7.0%
2.3	top	0.65 ± 0.05	$0.597 \pm 0.006 \pm 0.021 \pm 0.028$	0.551	$0.476 \pm 0.021 \pm 0.011$	0.284	6.2%
	short	0.30 ± 0.05	$0.560 \pm 0.009 \pm 0.026 \pm 0.067$	0.601	$0.322 \pm 0.017 \pm 0.021$	0.180	9.0%
2.0	top	0.65 ± 0.05	$0.605 \pm 0.004 \pm 0.016 \pm 0.030$	0.545	$0.495 \pm 0.020 \pm 0.010$	0.299	5.7%
	bottom	0.65 ± 0.05	$0.636 \pm 0.019 \pm 0.016 \pm 0.031$	0.560	$0.484 \pm 0.021 \pm 0.010$	0.308	6.4%
1.3	top	0.70 ± 0.05	$0.571 \pm 0.003 \pm 0.009 \pm 0.033$	0.509	$0.494 \pm 0.019 \pm 0.010$	0.282	5.7%
	bottom	0.70 ± 0.05	$0.535 \pm 0.003 \pm 0.010 \pm 0.028$	0.458	$0.493 \pm 0.019 \pm 0.010$	0.264	5.5%
	short	0.30 ± 0.05	$0.552 \pm 0.010 \pm 0.030 \pm 0.060$	0.581	$0.383 \pm 0.016 \pm 0.014$	0.211	10.2%
1.1	bottom	0.75 ± 0.10	$0.568 \pm 0.002 \pm 0.007 \pm 0.080$	0.563	$0.496 \pm 0.020 \pm 0.020$	0.282	11.1%

849 The EST prediction has been demonstrated to apply to the ¹⁵N
850 and H of the ammonia molecule by several experiments start-
851 ing with the Spin Muon Collaboration [52]. The SLAC E143
852 collaboration performed an empirical fit and showed [53]:

$$853 \quad P_{^{15}\text{N}} = 0.136|P_p| - 0.183|P_p|^2 + 0.335|P_p|^3, \quad (46)$$

854 which gives $P_{^{15}\text{N}} \approx -15\%$ when $P_p = 90\%$ and $P_{^{15}\text{N}} \approx$
855 -8.8% when $P_p = 70\%$. The ¹⁵N polarization is carried
856 by the unpaired proton and its effect relative to the three free
857 protons in NH₃ is

$$858 \quad \Delta P = \frac{1}{3} \left(-\frac{1}{3} \right) P(^{15}\text{N}), \quad (47)$$

859 where the additional factor of $-1/3$ comes from the wave-
860 function of the unpaired proton in the ¹⁵N [54]. The effect on
861 the asymmetry due to the polarized proton in the ¹⁵N is thus at
862 the $(1-2)\%$ level, and is negligible compared to the statistical
863 uncertainty of the asymmetry and the systematic uncertainty
864 due to the polarizations and the dilution factor.

865 H. Acceptance Corrections

866 When studying how the asymmetries vary with very small
867 bins in all four kinematic variables – the electron’s Q^2 , W
868 and the pion’s center-of-mass angles θ^* and ϕ^* – the effect of
869 the detector acceptance and efficiency in principle cancel and
870 therefore do not affect the interpretation of the asymmetry re-
871 sults. The effect of acceptance only becomes relevant when
872 integration of the asymmetry over a subset of these four vari-
873 ables is necessary, which is the case for all results presented
874 in Section IV.

875 For results presented in Section IV, we evaluated the ac-
876 ceptance of each bin based on acceptance cuts for both elec-
877 trons and pions. The acceptance correction was then applied

878 on an event-by-event basis: instead of using the measured
879 counts $N_{\uparrow\uparrow, \uparrow\downarrow, \downarrow\uparrow, \downarrow\downarrow}$, where each event counts as 1, we first
880 divided 1 by the acceptance of that particular event, then the
881 sum was taken and used as $N_{\uparrow\uparrow, \uparrow\downarrow, \downarrow\uparrow, \downarrow\downarrow}$ in the formula from
882 Section III E, Eqs. (37-39). The asymmetries extracted this
883 way were integrated over certain kinematic ranges and com-
884 pared directly with theoretical predictions. Zero-acceptance
885 bins could not be corrected this way when integrating the
886 data. When integrating the theoretical calculations, we ex-
887 cluded bins where there were no data, and thus removed the
888 zero-acceptance bins from the theory curves as well.

889 I. Radiative Corrections

890 Radiative corrections were calculated for both A_{UL} and
891 A_{LL} using the code EXCLURAD [55] and the MAID2007
892 model [13]. It was found that overall the correction is fairly
893 small and typically no larger than 0.03. Considering the size
894 of the statistical uncertainty of the measurement, radiative cor-
895 rections were not applied to the asymmetries, but rather are
896 quoted as a systematic uncertainty of $\Delta A = \pm 0.03$ through-
897 out the accessed kinematics.

898 J. Summary of All Systematic Uncertainties

899 The systematic uncertainty of the $\vec{e}\vec{p} \rightarrow e'\pi^+(n)$ exclu-
900 sive channel is dominated by that from the product $P_b P_t f_{\text{dil}}^{\pi^+}$,
901 shown in Table III. The uncertainty of $P_b P_t f_{\text{dil}}^{\pi^+}$ takes into
902 account the uncertainties in the target packing factor, as well
903 as the thickness and density of various materials in the target.
904 Other non-negligible systematic uncertainties include a relative
905 $\pm(1-2)\%$ due to the ¹⁵N in NH₃ and a ± 0.03 due to radia-

TABLE IV. Summary of systematic uncertainties due to the target and beam polarizations and the dilution factor for different beam and target combinations. The $(1 - 2)\%$ relative uncertainty due to ^{15}N and the ± 0.03 absolute uncertainty due to radiative corrections must be added in quadrature to the values here to obtain the total systematic uncertainty.

E_{beam} (GeV)	Target (NH_3)	$\Delta A_{UL}/A_{UL}$ (syst)	$\Delta A_{LL}/A_{LL}$ (syst)
3.0	top	7.0%	7.0%
2.3	top	6.2%	6.3%
	short	9.0%	9.0%
2.0	top	5.7%	5.8%
1.3	top	5.7%	5.9%
	bottom	5.5%	5.7%
1.1	bottom	11.1%	11.2%

tive corrections. Adding these uncertainties in quadrature, we arrive at Table IV for our asymmetry results. For the asymmetry A_{UL} , one does not need to normalize by P_b . We relied on the elastic $P_b P_t$ results and combined in quadrature their uncertainties with the uncertainty in the Møller polarization to obtain the uncertainty on P_t alone.

IV. ASYMMETRY RESULTS

Results for the target asymmetry A_{UL} and the double-spin asymmetry A_{LL} are available on a 4-dimensional grid of Q^2 , W , $\cos\theta^*$ and ϕ^* . There are 42 Q^2 bins logarithmically spaced between 0.00453 and 6.45 $(\text{GeV}/c)^2$, 38 W bins between 1.1 and 2.21 GeV/c^2 , 30 ϕ^* bins between 0 and 360°, and 20 $\cos\theta^*$ bins between -1 and 1. This binning scheme is referred to as “asymmetry bins”. To allow a meaningful comparison with theoretical calculations, we integrated the data over 3 Q^2 bins, 8 W bins, 5 ϕ^* bins and 5 $\cos\theta^*$ bins. These will be referred to as “combined bins” hereafter. The resulting combined W bins are (1.1, 1.34), (1.34, 1.58) and (1.58, 1.82) GeV/c^2 , allowing an examination of the first, the second, and the third nucleon resonance regions, respectively.

The method of integrating the data for the combined bins was built upon the acceptance correction described in Section IIIH: to correct for the acceptance, each event in the asymmetry bin was divided by the acceptance of that particular event, then summed to be used as $N_{\uparrow\uparrow, \uparrow\downarrow, \downarrow\uparrow, \downarrow\downarrow}$ in Eqs. (37-39). To integrate from asymmetry bins into combined bins, these acceptance-corrected $N_{\uparrow\uparrow, \uparrow\downarrow, \downarrow\uparrow, \downarrow\downarrow}$ from each asymmetry bin was summed, and used as the combined $N_{\uparrow\uparrow, \uparrow\downarrow, \downarrow\uparrow, \downarrow\downarrow}$ to evaluate the asymmetries for the combined bin. Using this method, the integrated asymmetries are direct reflections of the ratio of the physical cross sections integrated over the combined bin except for regions that had zero acceptance. To compare with theory, we calculated the cross sections $\sigma_{t,et,0}$ for each asymmetry bin, then summed the calculated

cross sections over combined bins except for asymmetry bins where there was no data (zero acceptance). The ratio of the summed cross sections [Eqs. (20-21)] was taken as the calculated asymmetry for the combined bin. In the following we will present some representative results.

A. Results on Target Asymmetry A_{UL}

Figure 13 shows, in increasing Q^2 ranges, the A_{UL} results as a function of W for three ϕ^* bins ($120^\circ, 180^\circ$), ($180^\circ, 240^\circ$), ($240^\circ, 300^\circ$), and integrated over $0.5 < \cos\theta^* < 1.0$. Results for the $\phi^* = (0^\circ, 60^\circ)$ and ($300^\circ, 360^\circ$) have less statistics and are not shown. Results for the $\phi^* = (60^\circ, 120^\circ)$ bin have comparable statistics as Fig. 13 but are not shown here for brevity. In general, we see that the agreement between these A_{UL} results and the four calculations, MAID2007 (solid) [13], JANR (dashed) [14], SAID (dash-dotted) [15], and DMT2001 (dotted) [16], is very good in the $W < 1.5$ (GeV/c^2) region, but for the region $1.5 < W < 1.8$ (GeV/c^2) , all four calculations differ from each other and none agrees well with data, although the MAID2007 curve (solid) approximates the data better than the other three.

To study these results further for different W regions, we show in Fig. 14 A_{UL} results as a function of ϕ^* for three W ranges and between $Q^2 = 0.0187$ and 0.452 $(\text{GeV}/c)^2$. Results for lower Q^2 ranges, down to 0.00646 $(\text{GeV}/c)^2$, are available from the 1.1 GeV data but only cover $1.2 < W < 1.5$ (GeV/c^2) and thus are not presented here. From Fig. 14, for the lower two W bins (1.12, 1.34) and (1.34, 1.58) GeV/c^2 , the four calculations provide similar predictions and all agree with data. But for the $W = (1.58, 1.82)$ GeV/c^2 region, only the MAID2007 (solid) and the DMT2001 (dotted) calculations provide the correct sign, and MAID2007 approximates the data better than the other three although it does not agree with data perfectly. It is clear that all four calculations can be improved in the $W > 1.58$ GeV/c^2 region throughout the Q^2 range shown.

B. Results on the Double-Spin Asymmetry A_{LL}

Figure 15 shows the double-spin asymmetry A_{LL} results as a function of W for eight Q^2 bins, three ϕ^* bins, and integrated over $\cos\theta^* = (0.5, 1.0)$. These results are compared with four calculations: MAID2007 (solid) [13], JANR (dashed) [14], SAID (dash-dotted) [15], and DMT2001 (dotted) [16]. Note that our definition for A_{LL} has opposite sign from theories, see Section IA. Results for the $\phi^* = (0^\circ, 60^\circ)$ and ($300^\circ, 360^\circ$) bins have less statistics and are not shown. Results for the $\phi^* = (60^\circ, 120^\circ)$ bin have comparable statistics as Fig. 13 but are not shown here for brevity. Overall the data agree very well with all four calculations. For all ϕ^* bins, the sign of A_{LL} in the region of the $N(1520)3/2^-$ and the $N(1680)5/2^+$ is positive in the high Q^2 , but start to cross or approach zero in the lower Q^2 bin, within (0.0919, 0.156) $(\text{GeV}/c)^2$ for $N(1520)3/2^-$ and within $Q^2 = (0.266, 0.452)$ $(\text{GeV}/c)^2$ for $N(1680)5/2^+$, re-

spectively. This is in agreement with the suggestion in Section I that A_{LL} turns to positive at high Q^2 values due to helicity conservation, but may become negative near the real photon point.

V. SUMMARY

We present here data on the target and double-spin asymmetry A_{UL} and A_{LL} on the $\vec{e}\vec{p} \rightarrow e\pi^+(n)$ channel using data taken on a polarized NH_3 target, from the EG4 experiment using CLAS in Hall B of Jefferson Lab. These data have reached a low Q^2 region from 0.0065 to 0.35 $(\text{GeV}/c)^2$ that was not accessed previously. They suggest a transition in A_{LL} from positive at higher Q^2 to negative values below $Q^2 \approx 0.1 (\text{GeV}/c)^2$ in the region $1.5 < W < 1.7 \text{ GeV}/c^2$, in agreement with both previous data from CLAS (high Q^2) [20, 22] and the real photon data at $Q^2 = 0$. Our results show that while all model calculations agree well with A_{LL} , in general there is room for improvements for A_{UL} in the high-mass resonance region

ACKNOWLEDGMENTS

The authors gratefully acknowledge the work of Jefferson Lab staff in the Accelerator and Physics Divisions that resulted in the successful completion of the experiment. This work was supported by: the U.S. Department of Energy (DOE), the U.S. National Science Foundation, the U.S. Jefferson Memorial Trust; the United Kingdom's Science and Technology Facilities Council (STFC) under grant numbers ST/L005719/1 and GR/T08708/01; the Italian Istituto Nazionale di Fisica Nucleare; the French Institut National de Physique Nucléaire et de Physique des Particules, the French Centre National de la Recherche Scientifique; and the National Research Foundation of Korea. Jefferson Science Associates, LLC, operates Jefferson Lab for the U.S. DOE under U.S. DOE contract DE-AC05-06OR23177.

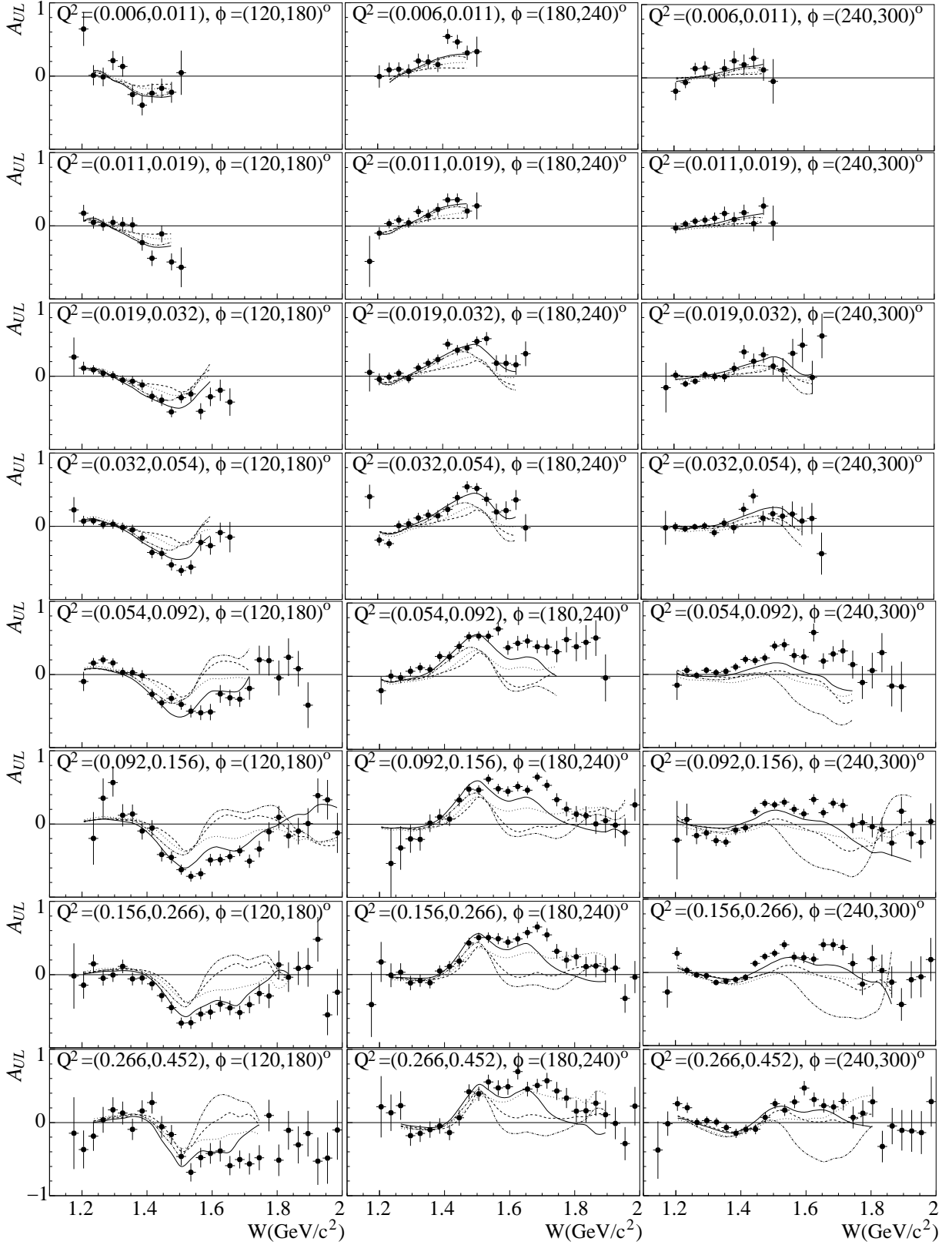


FIG. 13. Results on the target spin symmetries A_{UL} for the $\bar{e}p \rightarrow e\pi^+(n)$ channel as a function of the invariant mass W in GeV/c^2 , integrated over $\cos\theta^* = (0.5, 1.0)$, in increasing Q^2 ranges and three 60° ϕ^* bins. From top to bottom the Q^2 bins are (0.00646, 0.0110) and (0.0110, 0.0187) (1.1 GeV NH_3 long bottom target), (0.0187, 0.0317) and (0.0317, 0.054) (1.3 GeV NH_3 long top target), (0.054, 0.0919) (2.0 GeV NH_3 long top target), (0.0919, 0.156), (0.156, 0.266), and (0.266, 0.452) $(\text{GeV}/c^2)^2$ (3.0 GeV NH_3 long top target). From left to right the ϕ^* bins are $\phi^* = (120^\circ, 180^\circ)$, $(180^\circ, 240^\circ)$ and $(240^\circ, 300^\circ)$. In each panel, the horizontal scale is from 1.1 to 2 GeV/c^2 in W and the vertical scale is from -1 to 1 . Data are compared to four calculations: MAID2007 (solid) [13], JANR (dashed) [14], SAID (dash-dotted) [15], and DMT2001 (dotted) [16].

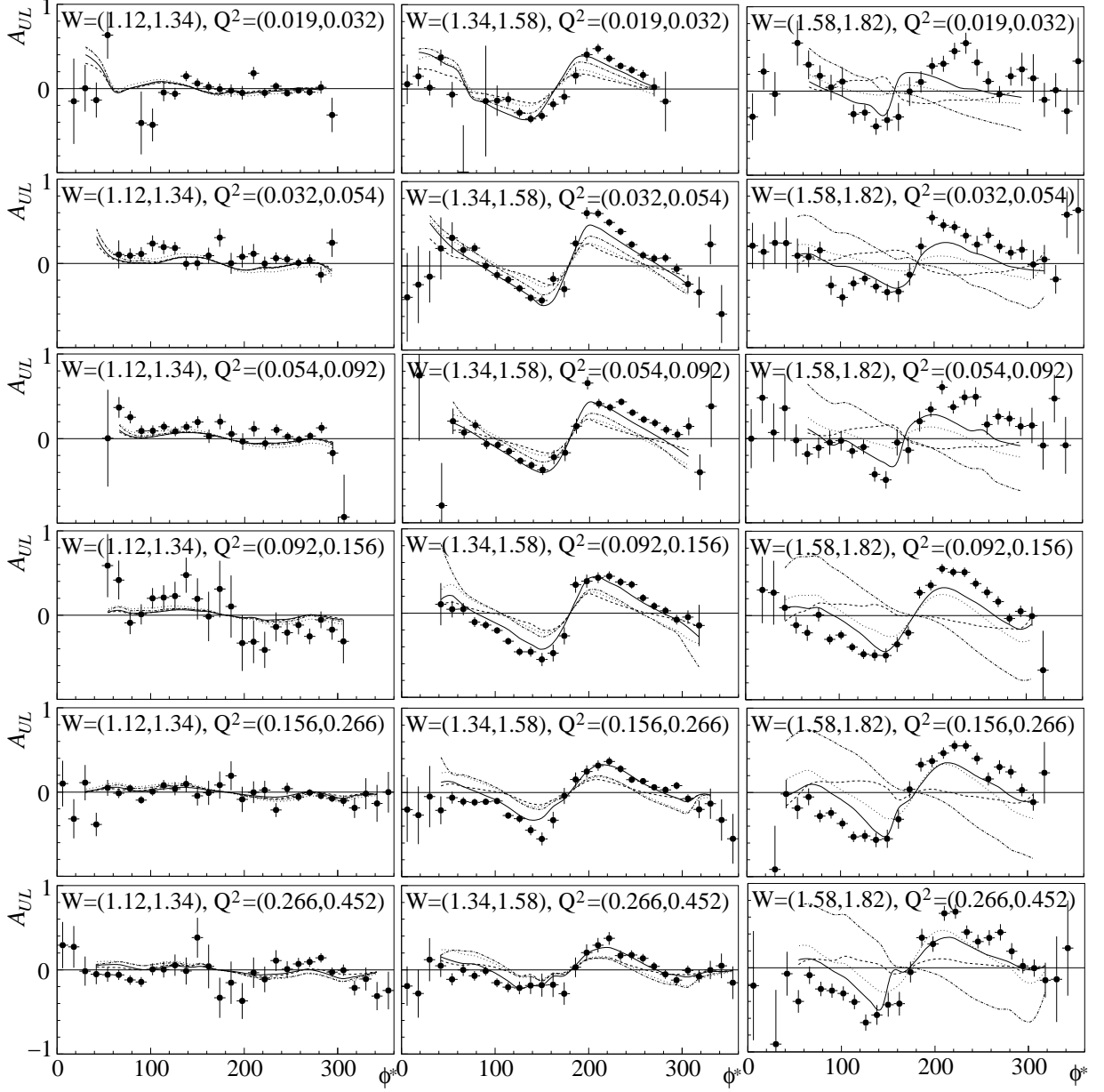


FIG. 14. Results on A_{UL} for the $\bar{e}p \rightarrow e\pi^+(n)$ channel as a function of azimuthal angle ϕ^* , integrated over $\cos\theta^* = (0.5, 1.0)$, for six Q^2 bins and three W bins. From top to bottom the six Q^2 bins are: $Q^2 = (0.0187, 0.0317)$ [1.3 NH₃ long target for $W = (1.12, 1.34)$ and $(1.34, 1.58)$ GeV/ c^2 , and 2.0 NH₃ long top target for $W = (1.58, 1.82)$ GeV/ c^2]; $(0.156, 0.266)$ and $(0.266, 0.452)$ (GeV/ c^2)² (2.0 GeV NH₃ long top target); $(0.0919, 0.156)$, $(0.156, 0.266)$ and $(0.266, 0.452)$ (GeV/ c^2)² (3.0 GeV NH₃ long top target); from left to right the W bins are: $W = (1.12, 1.34)$, $(1.34, 1.58)$, $(1.58, 1.82)$ GeV/ c^2 . In each panel, the horizontal scale is from 0 to 360° in ϕ^* and the vertical scale is from -1 to 1 . Data are compared to four calculations: MAID2007 (solid) [13], JANR (dashed) [14], SAID (dash-dotted) [15], and DMT2001 (dotted) [16].

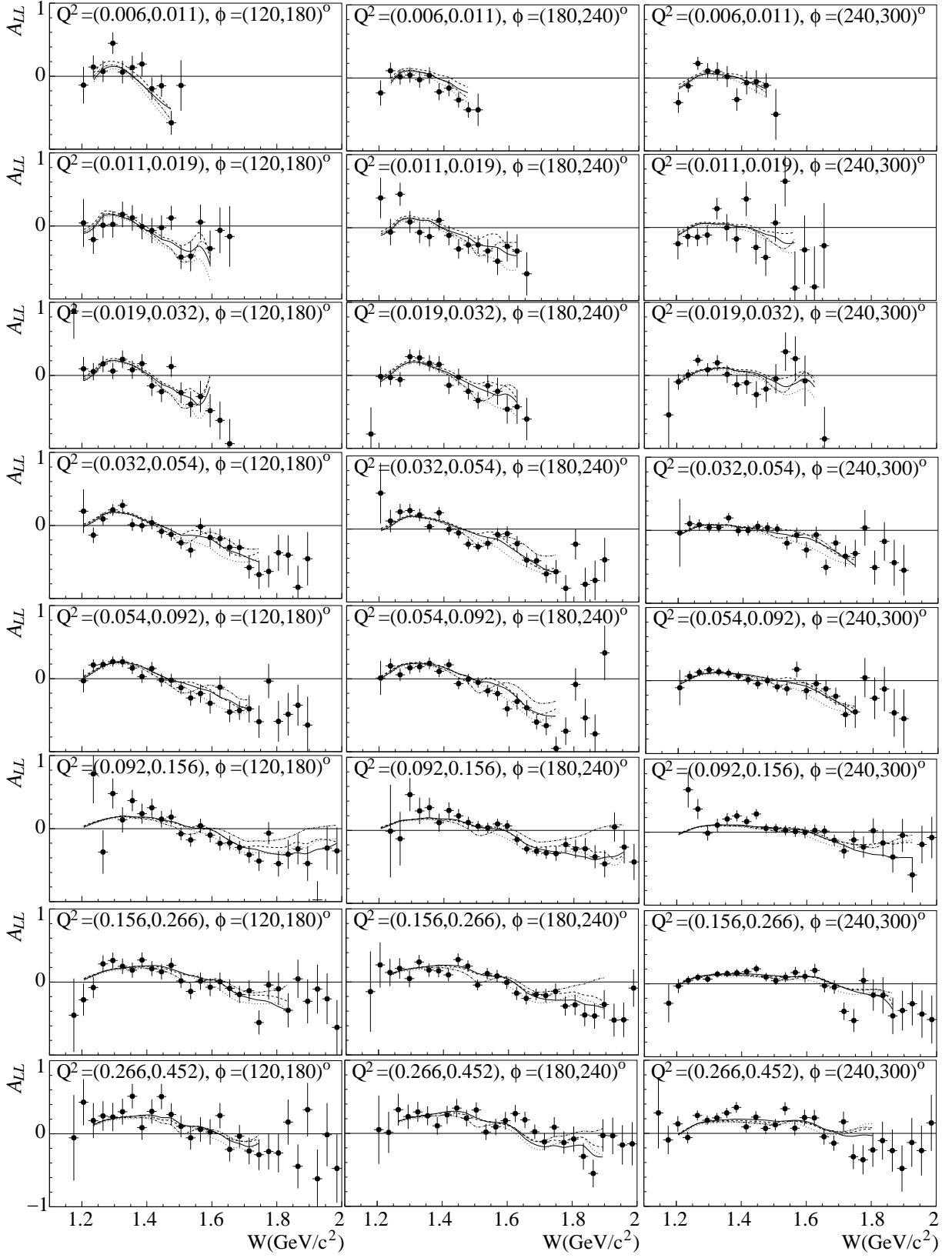


FIG. 15. Results on the double-spin symmetries A_{LL} for the $\bar{e}p \rightarrow e\pi^+(n)$ channel as a function of the invariant mass W in GeV/c^2 , integrated over $\cos\theta^* = (0.5, 1.0)$, for increasing Q^2 ranges and three 60° ϕ^* bins. From top to bottom the Q^2 bins are (0.00646, 0.011) and (0.011, 0.0187) (1.1 GeV NH_3 long bottom target), (0.0187, 0.0317) and (0.0317, 0.054) (1.3 GeV NH_3 long top target), (0.054, 0.0919) (2.0 GeV NH_3 long top target), (0.0919, 0.156), (0.156, 0.266), and (0.266, 0.452) $(\text{GeV}/c^2)^2$ (3.0 GeV NH_3 long top target). From left to right the ϕ^* bins are $\phi^* = (120^\circ, 180^\circ)$, $(180^\circ, 240^\circ)$ and $(240^\circ, 300^\circ)$. In each panel, the horizontal scale is from 1.1 to 2 GeV/c^2 in W and the vertical scale is from -1 to 1. Data are compared to four calculations: MAID2007 (solid) [13], JANR (dashed) [14], SAID (dash-dotted) [15], and DMT2001 (dotted) [16].

- [1] D. J. Gross and F. Wilczek, Phys. Rev. Lett. **30**, 1343 (1973).
- [2] H. D. Politzer, Phys. Rev. Lett. **30**, 1346 (1973).
- [3] V. D. Burkert and T. S. H. Lee, Int. J. Mod. Phys. E **13**, 1035 (2004).
- [4] I. G. Aznauryan and V. D. Burkert, Prog. Part. Nucl. Phys. **67**, 1 (2012).
- [5] C. Hoelbling, Acta Phys. Polon. B **45**, no. 12, 2143 (2014).
- [6] A. Ukawa, J. Statist. Phys. **160**, 1081 (2015).
- [7] V. Bernard, N. Kaiser, T. S. H. Lee and U. G. H. Meissner, Phys. Rept. **246**, 315 (1994).
- [8] V. Bernard, N. Kaiser and U. G. Meissner, Nucl. Phys. A **607**, 379 (1996) [Erratum-ibid. A **633**, 695 (1998)].
- [9] X. Zheng *et al.* [Jefferson Lab Hall A Collaboration], Phys. Rev. Lett. **92**, 012004 (2004).
- [10] X. Zheng *et al.* [Jefferson Lab Hall A Collaboration], Phys. Rev. C **70**, 065207 (2004).
- [11] M. Warns, W. Pfeil and H. Rollnik, Phys. Rev. D **42**, 2215 (1990).
- [12] V. D. Burkert, R. De Vita, M. Battaglieri, M. Ripani and V. Mokeev, Phys. Rev. C **67**, 035204 (2003).
- [13] D. Drechsel, S. S. Kamalov and L. Tiator, Eur. Phys. J. A **34**, 69 (2007).
- [14] I. G. Aznauryan *et al.* [CLAS Collaboration], Phys. Rev. C **80**, 055203 (2009).
- [15] The SAID partial wave analysis, R.A. Arndt *et al.*, URL: <http://gwdac.phys.gwu.edu/>; R. A. Arndt, W. J. Briscoe, M. W. Paris, I. I. Strakovsky and R. L. Workman, Chin. Phys. C **33**, 1063 (2009).
- [16] S. S. Kamalov and S. N. Yang, Phys. Rev. Lett. **83**, 4494 (1999).
- [17] R. De Vita *et al.* [CLAS Collaboration], Phys. Rev. Lett. **88**, 082001 (2002) [Erratum-ibid. **88**, 189903 (2002)].
- [18] R. De Vita [CLAS Collaboration], Nucl. Phys. A **699**, 128 (2002).
- [19] A. Biselli *et al.* [CLAS Collaboration], Phys. Rev. C **68**, 035202 (2003).
- [20] J. Pierce, Double Spin Asymmetry in Exclusive π^+ Electroproduction with CLAS, Ph.D. thesis, University of Virginia (2008).
- [21] S. Careccia, Single and Double Spin Asymmetries for π^- Electroproduction from the Deuteron in the Resonance Region, Ph.D. thesis, Old Dominion University (2012).
- [22] P. E. Bosted *et al.* [CLAS Collaboration], arXiv:1604.04350 [nucl-ex].
- [23] Particle Data Group, D.E. Groom *et al.*, Eur. Phys. J. C **15**, 1, (2000).
- [24] S. Capstick, Phys. Rev. D **46**, 2864 (1992).
- [25] M. Gottschall *et al.* [CBELSA/TAPS Collaboration], Phys. Rev. Lett. **112**, no. 1, 012003 (2014).
- [26] H. Iwamoto [CLAS Collaboration], AIP Conf. Proc. **1432**, 275 (2012).
- [27] D. Schott *et al.* [CLAS Collaboration], AIP Conf. Proc. **1735**, 030016 (2016).
- [28] JLab CLAS Experiment 04-102, D. I. Sober, M. Khandaker, D. G. Crabb, *Helicity Structure of Pion Photoproduction*.
- [29] JLab CLAS Experiment 03-006, M. Battaglieri, R. De Vita, A. Deur and M. Ripani, *The GDH Sum Rule with nearly real photons and the proton g_1 structure function at low momentum transfer*.
- [30] JLab Proposal 05-111, A. Deur, G. Dodge and K. Slifer, *Measurement of the Gerasimov-Drell-Hearn Integral at low Q_2 on the Neutron and Deuteron*.
- [31] S. B. Gerasimov, Sov. J. Nucl. Phys. **2**, 430 (1966) [Yad. Fiz. **2**, 598 (1965)].
- [32] S. D. Drell and A. C. Hearn, Phys. Rev. Lett. **16**, 908 (1966).
- [33] M. Anselmino, B. L. Ioffe and E. Leader, Sov. J. Nucl. Phys. **49**, 136 (1989) [Yad. Fiz. **49**, 214 (1989)].
- [34] X. Ji, C. W. Kao and J. Osborne, Nucl. Phys. A **684**, 363 (2001).
- [35] Hyekoo Kang, Measurement of the proton spin structure functions at very low momentum transfer, Seoul National University (2015).
- [36] B. A. Mecking *et al.* [CLAS Collaboration], Nucl. Instrum. Meth. A **503**, 513 (2003).
- [37] G. Adams *et al.*, Nucl. Instrum. Meth. A **465**, 414 (2001).
- [38] E. Cisbani *et al.*, Nucl. Instrum. Meth. A **496**, 305 (2003).
- [39] D. G. Crabb and D. B. Day, Nucl. Instrum. Meth. A **356**, 9 (1995).
- [40] C. D. Keith *et al.*, Nucl. Instrum. Meth. A **501**, 327 (2003).
- [41] J. S. Price *et al.*, 5-MeV Mott polarimeter for rapid precise electron beam polarization measurements, prepared for Conference: C96-09-10, p.727 Proceedings.
- [42] J. S. Price *et al.*, 5-MeV Mott polarimeter development at Jefferson Lab, In Urbana 1997, Polarized gas targets and polarized beams 446-450.
- [43] J. S. Price *et al.*, Recent measurements with the Jefferson Lab 5-MeV Mott polarimeter, In Protvino 1998, High energy spin physics 554-556.
- [44] M. Steigerwald, MeV Mott polarimetry at Jefferson Lab, http://www.jlab.org/accel/inj_group/mott/mott.pdf
- [45] K. Joo *et al.* [CLAS Collaboration], Phys. Rev. C **70**, 042201 (2004).
- [46] K. Park *et al.* [CLAS Collaboration], Phys. Rev. C **77**, 015208 (2008).
- [47] K. Adhikari, Measurement of the Spin Structure Function g_1^d of the Deuteron and Its Moments at Low Q^2 , Ph.D. thesis, Old Dominion University (2013).
- [48] CLAS-NOTE 2003-005, A. Klimenko and S. Kuhn, *Momentum Corrections for E_6* . http://www.jlab.org/Hall-B/notes/clas_notes03/03-005.pdf
- [49] J. Beringer *et al.* (Particle Data Group), Phys. Rev. D **86**, 010001 (2012).
- [50] P. E. Bosted, Phys. Rev. C **51**, 409 (1995).
- [51] R. De Vita, *Measurement of the Double Spin Asymmetry in π^+ Electroproduction with CLAS*, Ph.D. Thesis, Università di Genova (2000).
- [52] B. Adeva *et al.* [Spin Muon Collaboration], Nucl. Instrum. Meth. A **419**, 60 (1998).
- [53] K. Abe *et al.* [E143 Collaboration], Phys. Rev. D **58**, 112003 (1998).
- [54] O. A. Rondon-Aramayo, Phys. Rev. C **60**, 035201 (1999).
- [55] Radiative Corrections for Exclusive Reactions, A. Afanasev, *et al.*, Phys. Rev. D **66**, 074004, 2002; J. Gilfoyle *et al.*, URL: <http://www.richmond.edu/~ggilfoyl/research/RC/wvo.html>.